# ESTIMATING SENSIBLE HEAT FLUX FROM REMOTELY SENSED MODERATE RESOLUTION IMAGING SPECTRORADIOMETER (MODIS) DATA

BOIYO RICHARD KIPKEMBOI
[B.Ed. (Sc)]
I56/CE/11178/2007

A THESIS SUBMITTED IN PARTIAL FULFILLMENT OF THE REQUIREMENTS FOR THE AWARD OF THE DEGREE OF MASTER OF SCIENCE IN THE SCHOOL OF PURE AND APPLIED SCIENCES OF KENYATTA UNIVERSITY.

FEBRUARY, 2012

# DECLARATION

This thesis is my original work and has not been presented for the award of a degree or any other award in any other University. All sources of information have particularly been acknowledged by means of references.

**Boiyo Richard Kipkemboi** ……………… 02/02/2012
Department of Physics, Sign Date
Kenyatta University,
P.O. Box 43844–00100,
Nairobi, Kenya.

This thesis has been submitted for examination with our approval as University Supervisors.

**Dr. Collins Mito** ……………… 02/02/2012
Department of Physics, Sign Date
University of Nairobi,
P.O. Box 3019–00100,
Nairobi, Kenya.

**Dr. Charles Migwi** ……………… 02/02/2012
Department of Physics, Sign Date
Kenyatta University,
P.O. Box 43844–00100,
Nairobi, Kenya.

**Professor I.V.S. Rathore** ……………… 02/02/201
Department of Physics, Sign Date
Babu Banarsi Das University,
Lucknow–226021, India.

CHAIRMAN
PHYSICS DEPARTMENT

# DEDICATION

This thesis is dedicated to my beloved wife Beatrice and to our sons Andrew and Sterling.

# ACKNOWLEDGEMENTS

First and foremost, gratitude goes to Dr. Collins Mito who directed me towards the study of this topic. I am particularly very grateful for the extraordinary advice, guidance and concern accorded as I undertook this task. His vast knowledge in the research area of remote sensing and links with the research world were tremendously invaluable. Thank you for the valuable suggestions, corrections and encouragement during this manuscript preparation. I am profoundly very grateful to Dr. Migwi for the relentless guidance during the development stage of this work. His suggestions and corrections were vital towards improving this work. Thank you for the parental love and concern accorded during the most difficult times in my M.Sc. studies.

The entire fraternity of Kenyatta University offered me a conducive and supportive environment for this work. Thanks to the Vice Chancellor of Kenyatta University, Prof. Olive Mugenda, for the unlimited internet access that provided timely information. I am very grateful to all members of teaching and non teaching staff, Physics Department led by Dr. Migwi for their mental support during the entire study period. I am particularity very gratefully to Dr. Ambusso for the programming skills, in $C^{++}$, accorded which were later extended to MATtrix LABoratory (MATLAB). Thanks to Dr. Hashim for the valuable suggestions, challenges and critics which were very vital towards improving the quality of this work.

My special thanks, with all respect, goes to my family. I am too grateful to my wife Beatrice for the moral, psychological and financial support during the highly demanding and challenging moments that resulted into this work. To my parents,

siblings and relatives, thanks for your love and care throughout my studies. My due regards goes to my colleagues: Mayaka, Agora, Omucheni, Cheruiyot, Olwenya, Tuwei and Mungwang'a, just to mention a few. I would like to thank Broglio Space Centre (BSC) in Malindi, Kenya for providing the data set used in simulation. Thanks to Dr. Antonio Martínez from University of Lleida, Spain for providing validation data. I wish to sincerely thank the entire community of St Clares' Maragoli Girls secondary school, led by Sr. Mary Stephen, for their support and cooperation during the entire study period.

Last, but by all means supreme, I am inexpressibly thankful to the Almighty God, Who Has faithfully been by my side and my guide in the course of scaling the academic ladder. Even when there appeared *a long dark tunnel at the end of the visible light*, I obtained the resilience to embrace on from His unfailing, magnanimous, and providential friendship. To him I ascirbe all praise, honour and majesty.

It is unforgettable moments in my life to meet all of you.

# TABLE OF CONTENTS

## CHAPTER I

## INTRODUCTION

## CHAPTER 2

## LITERATURE REVIEW

## CHAPTER 3

## THEORETICAL BACKGROUND

## CHAPTER 4

## METHODOLOGY

## CHAPTER 5

## RESULTS AND DISCUSSIONS

## CHAPTER 6

## CONCLUSIONS AND RECCOMENDATIONS

## LIST OF TABLES

# LIST OF FIGURES

# ABBREVIATIONS AND ACRONYMS

| | |
|---|---|
| ASTER | Advanced Spaceborne Thermal Emission and Reflection radiometer |
| ATSR | Along–Track Scanning Radiometer |
| AVHRR | Advanced Very High Resolution Radiometer |
| BSC | Broglio Space Center |
| CRPSM | Centro di Ricerca Progetto San Marco |
| EOS | Earth Observing System |
| FASCODE | Fast Atmospheric Signature code |
| GSWT | General Split–Window Technique |
| HITRAN | High–resolution transmission molecular absorption |
| LAS | Large Aperture Scintillometer |
| LEO | Low Earth Orbiting |
| LST | Land Surface Temperature |
| MODIS | Moderate Resolution Imaging Spectroradiometer |
| MOS | Monin–Obukhov Similarity |
| NASA | National Aeronautic and Space Administration |
| NIR | Near Infra-Red |
| NOAA | National Oceanic and Atmospheric Administration |
| SRA | Surface Renewal Analysis |
| SST | Sea Surface Temperature |
| TIR | Thermal Infrared |
| TVDI | Temperature Vegetation Dryness Index |
| WVC | Water Vapor Column |

# LIST OF SYMBOLS

| | |
|---|---|
| $r$ | Aerodynamic resistance |
| $T_a$ | Air temperature |
| $T_4$ | Brightness temperature for AVHRR channel 4 |
| $T_5$ | Brightness temperature for AVHRR channel 5 |
| $T_{31}$ | Brightness temperature for MODIS band 31 |
| $T_{32}$ | Brightness temperature for MODIS band 32 |
| $\rho$ | Density of air |
| $G$ | Ground heat flux |
| $LE$ | Latent heat flux |
| $g$ | Acceleration due to gravity |
| $\bar{\bar{B}}_\upsilon$ | Downwelling atmospheric mean radiance |
| $\bar{B}_\upsilon$ | Upwelling atmospheric mean radiance |
| $R$ | Net radiation |
| $H$ | Sensible heat flux |
| $B_{\lambda,T}$ | Spectral emittance of a blackbody |
| $T_s$ | Surface temperature |
| $R_{sd}$ | Downward shortwave radiation |
| $u$ | Wind speed |
| $T_b$ | Brightness temperature |
| $d$ | Zero–plane displacement height |

# Abstract

Sensible heat flux $(H)$ has a high impact on energy exchange between the surface and atmosphere, climate change and climatic and hydrological modeling. In the past, remote sensing of $H$ has become a major area of interest and as a result, various methods have been established for its retrieval. However, large discrepancies between measured and simulated values of $H$ have been observed over land surfaces because of various assumptions and simplifications. This study presents a generalized algorithm for estimation of sensible heat flux that is suitable for a wide range of atmospheric and terrestrial conditions from Moderate Resolution Imaging Spectroradiometer (MODIS) data. MODIS is an adequate sensor to perform regional assessments by means of its high temporal and spatial coverage. Standard built–in atmospheric profiles in Fast Atmospheric Signature Code (FASCODE) together with atmospheric conditions obtained by periodic radiosounding, once a week, performed at Broglio Space Center (BSC) in Malindi, Kenya were used in simulating MODIS data at 11.03 μm and 12.02 μm wavelengths using PcLnWin software. The General Split Window Technique (GSWT) earlier proposed by Mito *et al.*, 2006 was modified by removing some of the assumptions it was originally based on, for example air temperature $(T_a)$ being approximately equal to surface temperature $(T_s)$, and used to retrieve surface temperature taking into account surface and air temperature difference effects, atmospheric water vapour and non–unitary surface emissivity. Formulation of sensible heat flux starting from the improved GSWT, bulk aerodynamic equation and the resulting aerodynamic resistance equation results in a general algorithm which relates sensible heat flux to the surface emittance effect, canopy properties, air temperature and different atmospheric stabilities. Unlike other conventional methods earlier developed for determination of sensible heat flux, a prior knowledge of the surface temperature as an auxiliary input is not necessary in this new algorithm. The estimates of sensible heat flux derived from MODIS using the proposed algorithm compared well with in situ measurements, obtained from Ebro River basin, Spain (41°18’04’’N, 0°’21’51”W, elevation 150 m), giving a good correlation coefficient of $r = 0.9$.

# CHAPTER 1

# INTRODUCTION

## 1.1 Background to the study

Sensible heat flux is the amount of heat energy transferred from the Earth's surface to the atmosphere by conduction and convection due to the temperature difference between them (Lu, 2009). Through sensible heat flux, the land absorbs heat energy from the atmosphere or releases heat energy to the atmosphere compensating the sharp temperature change in the atmosphere and regulating local climate. Accurate determination of sensible heat flux provides important scientific information for global energy change research and contributes greatly to the understanding of dynamic transfers of water, energy and trace gases at the Earth's surface (Watts *et al.*, 1998). Information about sensible heat flux is also important in modeling and monitoring of other energy balance components including net radiation, latent heat flux and ground heat flux.

A drastic climate change in the past has greatly increased the importance of global environmental study (Houghton *et al.*, 2001). A major focus has been the determination of the energy balance components of sensible heat flux, latent heat flux, ground heat flux and net radiation. Techniques for measuring these fluxes have improved in terms of methods, instrumentation and computation. Specifically, sensible heat flux has been determined by two techniques namely: instrumental measurements and mathematical models. Direct measurements, using instruments like Large Aperture Scintillometer (LAS) and Surface Renewal Analysis (SRA), have been reported to have various limitations including precision errors, high expertise and high cost, with the latter limited to intensive field experiments (Watts *et al.*, 2000). These methods also provide estimates of sensible heat flux with low temporal resolution. The use of mathematical models, on the other hand, has drawn mixed results in spite of the similarity in input variables (Allen *et al.*, 2005). Most estimates have reported a wide range of discrepancies when compared to measured values (Chehbouni *et al.*, 1997).

Remote sensing technology using a high resolution, multi–bands, multi–temporal and multi–angular remote sensing instruments has brought the hope of estimating sensible heat flux over different surfaces (Liu *et al.*, 2007). Efforts have been devoted to investigate parametization of sensible heat flux and to improve on its accuracy using measurements at various spatial and temporal resolutions and over various land surfaces. Therefore, compared with other methods, remote sensing has obvious superiority to estimate sensible heat flux over different surface conditions.

However, major challenges exist in retrieving accurate and reliable values of sensible heat flux by this technique. First, retrieving accurate estimates of surface temperature from satellite data and to be able to extrapolate them temporally and second, relating estimates of sensible heat flux obtained over relatively large surfaces from satellite data, 1 km$^2$ to 16 km$^2$, to ground measurements usually representative of less than 0.1 km$^2$ (Watts *et al.*, 1998).

Sensible heat flux depends directly on the difference between surface and air temperature and hence its accurate determination requires good knowledge of these parameters. Large scale retrieval of surface temperature from satellite measurements in the thermal infrared is not an easy task because of high heterogeneity over short distances, mainly due to vegetation, topography and soil physical properties and the complex relationship between atmosphere and the surface (Sobrino *et al*., 2008). Surface temperature varies spatially according to soil type, soil moisture, land use and land cover and temporally with time of the day and season of the year (Lu, 2009). Hence the use of meteorologically obtained surface temperature to estimate sensible heat flux is inappropriate.

The assumption that surface temperature $(T_s)$ is equal to air temperature $(T_a)$, as made by most studies, is not appropriate in the estimation of sensible heat flux. Such assumption negates the concept of the sensible heat flux as $H$ depends directly on the difference between the two temperatures. Air temperature can differ more or less significantly from surface temperature depending on the solar and view geometry, soil moisture, wind speed and direction and particularly vegetation cover and structure of the surface (Chehbouni *et al*., 1997, Kustas and Craig, 1990). Surface temperature corresponds to a weighted soil and canopy temperature while $T_a$ relates to the efficiency of heat exchange between the land surfaces and overlying atmosphere.

Since sensible heat flux has a large diurnal variation and is subject to significant variation from one day to another, a high frequency repeat rate is required. This is only available on wide swath sensors on Low Earth Orbiting (LEO) satellites like Advanced Very High Resolution Radiometer (AVHRR) on board the National Oceanic and Atmospheric Administration (NOAA) series satellites and MODIS on board the Terra and Aqua satellites. MODIS is a payload polar orbiting satellite launched into the Earth orbit by National Aeronautic and Space Administration

(NASA) Goddard Space Flight Center (GSFC) on 18th December, 1999 on board the Terra platform satellite, and second on 4th May, 2002 on board the Aqua platform satellite (Mallick *et al*., 2009). Some advantages of the instrument include its global coverage and high radiometric resolution (Xiong *et al*., 2008). Being on Terra and Aqua satellites, MODIS data can be acquired four times a day for the same area: Aqua passes south to north over the equator in the afternoon (at local times 1.30 p.m., ascending mode) and in the morning (local times 1.30 a.m., descending mode), while Terra overpasses from north to south across the equator in the morning (at local times of 10.30 a.m., descending mode) and in the afternoon (10.30 p.m., ascending mode) (Wang and Liang, 2009). Terra is at an altitude of 750 km and has a cross and a long track swath of 2330 km and 10 km respectively (Abreham, 2009). Terra and Aqua MODIS instruments are effectively the same, although band 31 on the Aqua MODIS saturates at a temperature of about 60 K below that for Terra (~400 K) (Hall *et al*., 2008).

MODIS acquires data in 36 spectral bands (Table 1.1) ranging in wavelength from 0.4 μm to 14.4 μm, and at varying spatial resolutions (2 bands at 250 m, 5 bands at 500 m and 29 bands at 1 km). These data improves the understanding of global dynamics and processes on the land, in the oceans, and in the lower atmosphere (Mito *et al*., 2006). Bands 1–19 and band 26 are in the visible and Near Infra–Red (NIR) range and the remaining bands are in the Thermal Infra–Red (TIR). The bands in the transparent atmospheric windows are designed for remote sensing of surface properties. Other bands are mainly for atmospheric studies.

**Table 1.1: Specifications of MODIS bands, (Wan and Li, 1997)**

| Band | Bandwidth (nm) | IFOV | Primary use | Band | Bandwidth (μm) | IFOV | Primary Use |
|---|---|---|---|---|---|---|---|
| 1 | 620-670 | 250m | L | 20 | 3.660-3.840 | 1km | O,L |
| 2 | 841-876 | 250m | A, L | 21 | 3.929-3.989 | 1km | fire, |
| 3 | 459-479 | 500m | L | 22 | 3.929-3.989 | 1km | volcano |
| 4 | 545-565 | 500m | L | 23 | 4.020-4.080 | 1km | A,L |
| 5 | 1230-1250 | 500m | L | 24 | 4.433-4.498 | 1km | A,L |
| 6 | 1628-1652 | 500m | A, L | 25 | 4.482-4.549 | 1km | A |
| 7 | 2105-2155 | 500m | A, L | 27 | 6.535-6.895 | 1km | A |
| 8 | 405-420 | 1km | O | 28 | 7.175-7.475 | 1km | A |
| 9 | 438-448 | 1km | O | 29 | 8.400-8.700 | 1km | A |
| 10 | 483-493 | 1km | O | 30 | 9.580-9.880 | 1km | L |
| 11 | 526-536 | 1km | O | 31 | 10.780-11.280 | 1km | ozone |
| 12 | 546-556 | 1km | O | 32 | 11.770-12.270 | 1km | A, L |
| 13 | 662-672 | 1km | O | 33 | 13.185-13.485 | 1km | A, L |
| 14 | 673-683 | 1km | O | 34 | 13.485-13.785 | 1km | A, L |
| 15 | 743-753 | 1km | O | 35 | 13.785-14.085 | 1km | A |
| 16 | 862-877 | 1km | O | 36 | 14.085-14.385 | 1km | A |
| 17 | 890-920 | 1km | A |  |  |  | A |
| 18 | 931-941 | 1km | A |  |  |  |  |
| 19 | 915-965 | 1km | A |  |  |  |  |
| 26 | 1360-1390 | 1km | Cirrus |  |  |  |  |

Note: A–atmospheric studies; L–land studies; O–ocean studies

Figure 1.1 illustrates the spectral transmittance values, in the 750 $cm^{-1}$ to 1050 $cm^{-1}$ region, corresponding to the most absorbing atmospheric gases: water vapour ($H_2O$), ozone ($O_3$) and carbon dioxide ($CO_2$) together with the relative response functions of AVHRR channels 4 (Ch 4) and 5 (Ch 5) and MODIS bands 31 (Ba 31) and 32 (Ba 32).

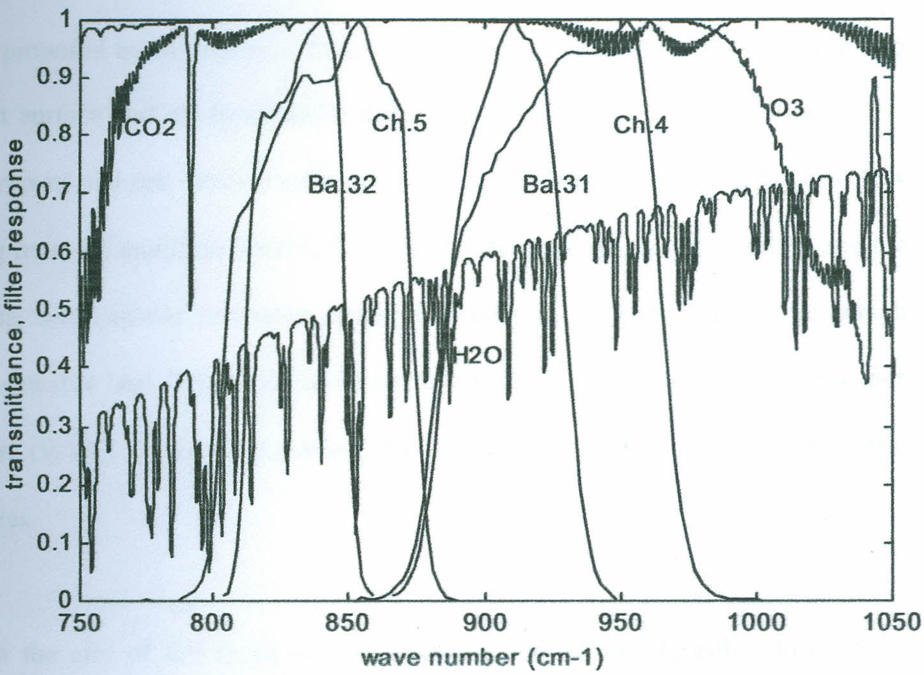

**Figure 1.1: Absorption of the atmospheric constituents and filter response of AVHRR/2 and MODIS, (Mito *et al.*, 2006)**

It can be seen that all spectral regions are affected by absorption in the atmosphere. However in the ranges of atmospheric window 800 cm$^{-1}$ to 950 cm$^{-1}$, the Earth's atmosphere is largely transparent and water vapour is the highly absorbing atmospheric gas. It is also evident how MODIS bands 31 and 32 reproduce very well the AVHRR channels 4 and 5, which have traditionally been used for remote sensing of Sea Surface Temperature (SST) and Land Surface Temperature (LST). The spectral ranges (Figure 1.1) of the two bands are closer to each other compared to those of AVHRR channels 4 and 5.

This study presents a generalized algorithm suitable for a wide range of atmospheric and terrestrial conditions to estimate sensible heat flux, one of the components of the surface energy balance, from MODIS data. The approach retrieves surface temperature using a modified form of the General Split Window Technique (GSWT) earlier proposed by Mito *et al.*, 2006. The modified algorithm does this taking into account surface and air temperature difference effects, in addition to atmospheric water vapour and non–unitary surface emissivity. Formulation of sensible heat flux starting from the modified GSWT, the bulk aerodynamic resistance equation and the resulting aerodynamic resistance equation results in a general algorithm which relates sensible heat flux to the surface emittance effect, atmospheric Water Vapor Column (WVC), canopy properties, air temperature and different atmospheric stabilities.

Though the aim of this study was the development of an algorithm to estimate sensible heat flux from MODIS data, its performance depends on accurate simulation and evaluation of a number of atmospheric effects. Coefficients which take into account different atmospheric stabilities were solved, by linear regression analysis with least–square–sum fitting using 21 sets of emissivity conditions. Since they were scarcely influenced by atmospheric water vapour content within the range 0.4–3.0 g $\text{cm}^{-2}$, their mean values were considered in evaluating coefficients appearing in the sensible heat flux algorithm. For any realistic amount of atmospheric water vapour content above this range, various regressive relationships were evaluated expressing these coefficients as functions of atmospheric water vapour. With aerodynamic resistance computed from canopy properties, emissivity conditions and water vapor column determined from satellite data, air temperature becomes the only auxiliary measurement required to compute sensible heat flux. Unlike other conventional methods earlier developed for determination of sensible heat flux, a prior knowledge of surface temperature as an auxiliary input is not necessary in this new algorithm.

Sensible heat flux has been validated with *in situ* data from Spain for the year 2004 for different days ranging from 15th April, 2004 to 26th July, 2004. The results showed that MODIS based sensible heat flux was highly correlated to *in situ* sensible heat flux, with a cumulative correlation coefficient for all the three conditions being 0.9.

## 1.2 Statement of the research problem

Direct measurement of sensible heat flux using meteorological instruments is expensive, time consuming and difficult. They also provide estimates of sensible heat flux with low spatial and temporal resolution. Existing models to estimate sensible heat flux have reported a wide range of discrepancies when compared to measured values because of various assumptions and simplifications. Remote sensing of sensible heat flux requires accurate values of surface and air temperatures as auxiliary measurements. Large scale retrieval of surface temperature from satellite measurements in the thermal infrared is not an easy task. This is because of high heterogeneity over short distances due to vegetation, topography and soil physical properties and the complex relationship between atmosphere and the surface. The assumption that surface temperature is equal to air temperature, as made by most models, is not appropriate in the estimation of sensible heat flux since $H$ depends directly on the difference between the two temperatures. This study was devoted to the development of an algorithm for estimation of sensible heat flux from

MODIS data on the basis of surface emittance effect, water vapor column (WVC), canopy properties and air temperature.

## 1.3 Objectives of the study

### 1.3.1 Main objective

The main objective of this study was to develop an algorithm to estimate sensible heat flux from remotely sensed Moderate Resolution Imaging Spectroradiometer (MODIS) data.

### 1.3.2 Specific Objectives

To achieve the main objective, two major steps were to be implemented:

a) Simulate atmospheric effects using PcLnWin software.
b) Improve the General Split Window Technique (GSWT) for retrieval of surface temperature from MODIS data.

## 1.4 Rationale

Sensible heat flux measurements in the thermal infrared continue to attract the attention of many scientific researchers. Its accurate measurements, for instance, is used in the fields of hydrology, forestry, metrology, global climate studies and vegetation monitoring. Major challenges have been reported in the use of meteorological instruments to estimate sensible heat flux (Chehbouni *et al.*, 1997). Conventional models earlier developed for its determination are based on some assumptions and simplifications, for example surface temperature being equal to air temperature and either one of the energy balance components being negligible, which are not appropriate in the estimation of sensible heat flux. Therefore, there was need to develop a general algorithm that can be applied to estimate sensible heat flux for a wide range of atmospheric and terrestrial conditions.

# CHAPTER 2

# LITERATURE REVIEW

## 2.1 Introduction

Significant progress has been made to estimate sensible heat flux using various techniques. These techniques have evolved in terms of methods, instrumentations and computations with remote sensing of sensible heat flux in the thermal infrared being a recent innovation. This chapter describes and summarizes the literature with respect to the present work. It discusses work which has already been done to estimate sensible heat flux, its contribution to the current research and the knowledge gap. A brief overview of surface temperature is also made.

## 2.2 Previous work on estimation of sensible heat flux

Two methods have been proposed to estimate sensible heat flux. They include: mathematical models and direct instrumental measurements.

### 2.2.1 Mathematical models

Watts *et al.*, 1998 estimated sensible heat flux using AVHRR channels 4 and 5. Data used included vegetation characteristics, air and surface temperatures. The bulk aerodynamic formula was used with surface temperature retrieved by the GSWT proposed by Uliveri *et al.*, 1994:

$$T_S = T_4 + 2.76(T_4 - T_5) + 38.6(1 - \bar{\varepsilon}) - 96.0\,\delta\varepsilon \tag{2.1}$$

where $T_S$ is the surface temperature, $T_4$ and $T_5$ are brightness temperatures of AVHRR channels 4 and 5 respectively, $\bar{\varepsilon} = (\varepsilon_{31} + \varepsilon_{32})/2$ and $\delta\varepsilon = \varepsilon_1 - \varepsilon_2$ are the mean and difference in emissivities respectively of AVHRR channels 4 and 5. Air temperature was obtained from meteorological stations and aerodynamic resistance approximated to a constant value (with inclusion of stability effects). Reasonable instantaneous estimates of $H$ were obtained, although with a large scatter.

Yamaguchi *et al.*, 2004 analyzed sensible heat flux in urban areas using Advanced Spaceborne Thermal Emission and Reflection Radiometer (ASTER) and MODIS data. Surface temperature was observed by ASTER, air temperature measured at ground meteorological stations, net radiation estimated from solar irradiance derived from ASTER data and ground heat flux inferred from net radiation and surface types. The assumption that latent heat flux is zero was inappropriate since it constitutes a major component of the energy balance.

Garcia and Sergio, 2005 developed a model for calculating energy fluxes in semi arid regions. Surface and air temperatures were evaluated at eleven meteorological stations. Sensible heat flux was calculated using the bulk aerodynamic resistance equation (Chehbouni *et al.*, 1997):

$$H = \frac{\rho C_p (T_s - T_a)}{r} \tag{2.2}$$

where $H$ is sensible heat flux (Wm$^{-2}$), $\rho$ is air density (kgm$^{-3}$), $C_p$ is specific heat capacity of air at constant pressure (Jkg$^{-1}$K$^{-1}$), $T_s$ is surface temperature (K), $T_a$ is air temperature (K) and $r$ is aerodynamic resistance (sm$^{-1}$). Though the overall adjustments were good, the $T_a$ estimates were subjected to local errors, because of the effects of the altitude among other factors. Numerical values of sensible heat flux obtained from ASTER and MODIS were compared to those obtained by Eddy Covariance (EC) measurements. Both ASTER and MODIS were found to underestimate sensible heat flux, as seen from Table 2.1.

**Table 2.1: Comparison between measured and estimated values of $H$, (García and Sergio, 2005)**

| | Sensor | H (Wm$^{-2}$) |
|---|---|---|
| Values | ASTER | 107.65 |
| | MODIS | 84.42 |
| | Measured | 152.98 |
| Error difference | ASTER-Measured | -45.33 |
| | MODIS-Measured | -68.56 |
| | MODIS-ASTER | -23.23 |

García *et al.*, 2008 estimated sensible heat flux using Temperature Vegetation Dryness Index (TVDI) and MODIS data. Their work assumed that ground heat flux (G) was negligible. This assumption is inappropriate since in some cases, ground heat flux ranges from 10% to 50% of the net radiation depending on the amount of vegetative cover (Kustas and Craig, 1990). On a well–watered and full–vegetation covered surface, ground heat flux is of the same order in magnitude as the sensible heat flux.

Samuel *et al.*, 1996 studied on daytime variation of sensible heat flux estimated by bulk aerodynamic resistance method over a grass canopy. Data used included air temperature, air vapor pressure, wind speed, net radiation, soil heat flux, incoming and reflected solar radiation, surface temperature and volumetric soil moisture content. Surface temperature was measured directly using infrared temperature transducer. The accuracy of the bulk aerodynamic method was tested with indirect measurements of sensible heat flux, derived from Bowen ratio energy method. Though there was a fair agreement between the two, there was a greater uncertainty on the method used to retrieve surface temperature.

Jiayi *et al.*, 2003 developed a model to estimate sensible heat flux under unstable conditions using satellite vector winds. The physical idea of the method is that air–sea temperature difference is related to the atmospheric convergence. Employed data included wind convergence, sea level humidity and sea surface temperature. The use of sea surface temperature represents some level of simplicity due to the fact that air temperature can be assumed to be equal to surface temperature without much errors being realized. Furthermore, the values of emissivities are well known and can be approximated to unity. Such assumptions are not applicable over land surfaces.

### 2.2 2. Direct instrumental methods

Instruments used to measure sensible heat flux are of two types: Large Aperture Scintillometer (LAS) and Surface Renewal Analysis (SRA). Many researchers have made direct measurement of sensible heat flux using LAS (Meijninger and De Bruin, 1999, Chehbouni *et al.*, 2000, De Wekker, 1996, De Bruin *et al.*, 1996 and Cain *et al.*, 2000). The model used to estimate sensible heat flux is given by (Chehbouni, 2000):

$$H = \rho C_p \, b(z-d)\left(\frac{g}{T}\right)^{\frac{1}{2}} (C_T^2)^{\frac{3}{4}} \tag{2.3}$$

where $T$ is the absolute temperature (K), $z$ is the path height above the ground (m), $d$ is the zero–plane displacement height (m), $\rho$ is the density of air (kgm$^{-3}$), $C_p$ is the specific heat capacity of air at constant pressure (Jkg$^{-1}$K$^{-1}$), $b = 0.57$ is an empirical constant, $g$ is the acceleration due to gravity (ms$^{-2}$) and $C_T$ is the structure parameter of temperature. Data required include wind speed, temperature (both obtained from meteorological stations) and $C_T^2$ (derived from scintillometer). The method has been found to be ineffective over a heterogeneous terrain (Cain *et al.*, 2000).

Paw *et al.*, 1995 developed the following model to estimate sensible heat flux by Surface Renewal Analysis (SRA):

$$H = \alpha \rho C_p \frac{a}{l+s} z_l \tag{2.4}$$

where $\alpha$ is a constant which accounts for uneven heating within the volume, $z_l$ is the height of the air volume (m), $l$ is the length of time during which the air parcel is being heated (s), $s$ is the quiescent period of time duration ramp events (s) and $a$ is the amplitude of the ramp events (m). The SRA, though the simplest method, provides reliable estimates of sensible heat flux but with low temporal resolution (Anandakumar, 1999).

## 2.3 Land Surface Temperature

Land Surface Temperature (LST) is a fundamental quantity in the physical description of energy fluxes. It is regarded as the surface skin temperature which is inferred from thermal emission of the Earth surface measured by a radiometer based on Planck's law (Lu, 2009). The satellite sensor measures Infrared radiance leaving the top of the atmosphere towards the satellite. This radiance is corrected with respect to the influence of a clear (i.e. nearly non–scattering) atmosphere. The resulting radiance is converted to a temperature according Planck's law called LST.

LST is not only a good indicator of the energy equilibrium at the Earth's surface, but also plays a direct role when estimating sensible heat flux (Tang *et al.*, 2008). Because of this, it is crucial to have access to reliable estimates of LST over large spatial and temporal scales. While it is practically impossible to obtain such information from ground based measurements, satellite observations in the Thermal Infra–Red (TIR) appears to be very attractive since it can give access to global estimates of LST.

Studies to retrieve LST have been carried using different sensors, mostly focusing on the use of polar orbiting satellites because of their high spatial resolution of about 1 km (Abreham, 2009). Examples include NOAA–AVHRR (Uliveri, 1994), Along–Track Scanning Radiometer (ATSR) (Sobrino *et al.*, 1993) and MODIS (Wan and Dozier, 1989, Mito *et al.*, 2006). According to radiometric channels used they are broadly grouped into 3 categories: single channel algorithm, split window algorithm and multi–band algorithm.

The split window technique is based on the differential water vapor absorption in two adjacent IR channels, usually within 10 – 12.5 μm window regions, to correct atmospheric effects (Uliveri *et al.*, 1994). The atmospheric attenuation is greater in one channel than the adjacent channel, and as the attenuation increases (as a result of increasing atmospheric water vapor, primarily), the difference in the radiance measured in the two bands increases (Ouaidrari *et al.*, 2002). Since the surface source of the radiance does not change between the bands, the different shift in sensor–measured radiance originates from atmospheric attenuation.

Various Split Window Techniques have been proposed by different researchers for retrieval of LST. Ulivieri *et al.*, 1994 developed the split window algorithm, equation 2.1, to retrieve LST using AVHRR. The algorithm was found to be accurate compared to several others and takes into account atmospheric effects, in particular the water vapour column amount and a non–unitary surface emissivity (Mito *et al.*, 2006). However, it is based on some assumptions, for example air temperature being approximately equal to surface temperature, which makes it possible to eliminate the third corrective term.

Mito *et al.*, 2006 modified Ulivieri's algorithm using MODIS data. From simulations it was possible for them to determine a third corrective term appropriate to MODIS bands 31 and 32, which takes into account the interdependence between water vapour and non–unitary emissivity. The algorithm developed has the formulation:

$$T_S = T_S' + H_1(1-\bar{\varepsilon}) + H_2\delta\varepsilon + H_3((1-\bar{\varepsilon})^2 - (0.5\delta\varepsilon)^2) \qquad (2.5)$$

where:

$$T_s' = T_{31} + 2.23(T_{31} - T_{32}) \tag{2.6}$$

where $T_{31}$ and $T_{32}$ are the brightness temperatures of MODIS bands 31 and 32 respectively, $H_1$, $H_2$ and $H_3$ are the split window coefficients, $\overline{\varepsilon} = (\varepsilon_{31} + \varepsilon_{32})/2$ and $\partial\varepsilon = \varepsilon_{31} - \varepsilon_{32}$ are the mean and difference in emissivities respectively of MODIS bands 31 and 32. However, their derivation assumed that surface temperature is equal to air temperature, making it possible to eliminate the fourth corrective term.

In this study, the algorithm proposed by Mito *et al.*, 2006 is further modified by including the fourth corrective term and used to retrieve sensible heat flux. The modified GSWT algorithm takes into account surface and air temperature difference effects in addition to atmospheric effects, in particular the WVC amount, and non–unitary surface emissivity. Other assumptions earlier made by most researchers in the estimation of sensible heat flux, for example; ground heat flux and latent heat flux being equal to zero, are not considered in the proposed study.

# CHAPTER 3

# THEORETICAL BACKGROUND

## 3.1 Introduction

This chapter considers comprehensively the concepts of global energy balance, surface energy balance components, thermal radiation, the basic land surface temperature equation and the aerodynamic resistance that forms the theoretical and scientific core of the study.

## 3.2 Global energy balance

This is the balance between incoming solar radiation (short wavelength radiation) and outgoing radiation from the Earth's atmosphere (long wavelength radiation). The global energy balance regulates the state of the Earth's climate. The energy balance is made up of three parts: solar incident energy, solar reflected energy and Earth emitted energy.

The energy released from the Sun as electromagnetic radiation corresponds to that emitted by a body having a surface temperature of 6000°C. At this temperature, electromagnetic radiation is emitted as shortwave light and ultraviolet energy and travels across the space at the speed of light. This incoming solar radiation is absorbed by the Earth's surface, gases (water vapour, ozone, carbon dioxide and carbon monoxide) and aerosols in the atmosphere. The incoming solar radiation is also reflected by the Earth's surface, clouds and the atmosphere. Reflection significantly affects solar radiation that reaches the ground. Absorbed energy is emitted by the Earth's atmosphere system as long wave radiation, since the Earth is much cooler than the Sun. The energy received by the Earth from the Sun balances the energy lost by the Earth back into space. In this way, the Earth maintains a stable average temperature and therefore a stable climate.

Pidwirny (2006) describes the global energy balance (Figure 3.1). Of the 100 units of solar radiation incident on the Earth surface, 19 units are absorbed, and therefore transferred into heat energy and longwave radiation in the atmosphere by two processes: 16 in a cloud–free air and 3 in clouds.

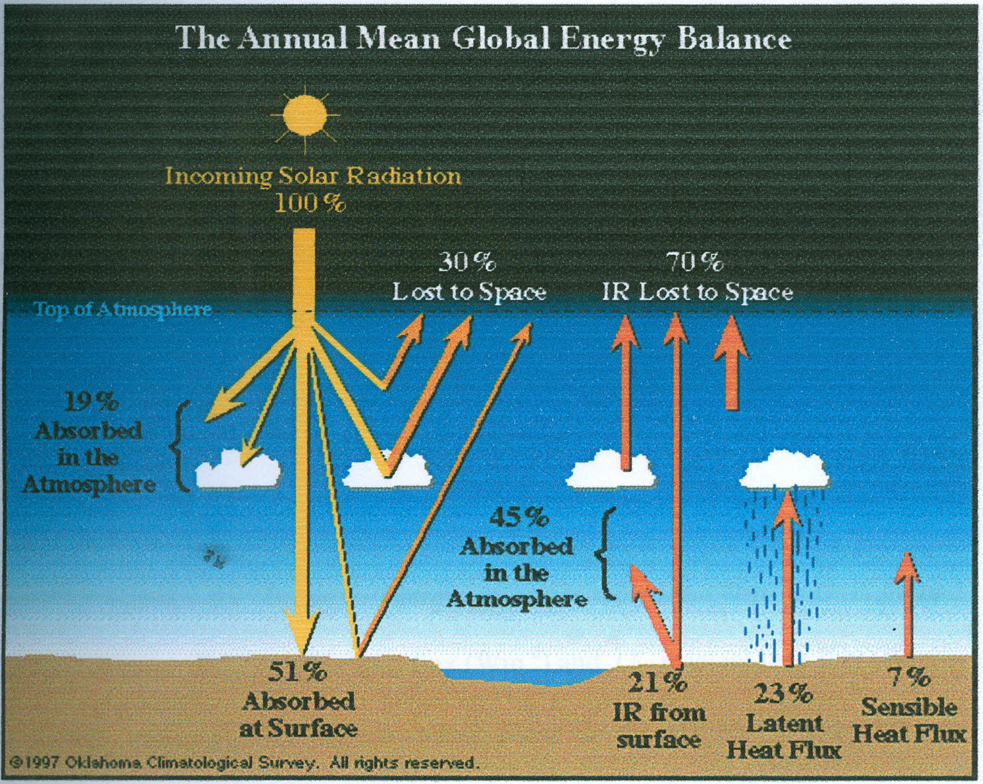

Figure 3.1: The Global energy balance, (Pidwirny, 2006)

Reflection of solar radiation back to space constitutes 30 units, which occur in three main ways: 4 units from surface reflection, 20 units from cloud reflection and 6 units from back scattering. The remaining 51 units of solar radiation are absorbed at the surface and eventually disposed by a combination of infrared radiation, sensible heat flux and latent heat flux amounting to 21 units, 15 units and 6 units respectively. Out of the 21 units of infrared radiation absorbed, 15 units are absorbed on passing through the atmosphere and 6 units reach the space. The remaining 30 units are transferred from the surface to the atmosphere by a combination of latent and sensible heat flux.

### 3.3 Surface energy balance components

In the places where there is no heating source from the interior of the Earth, natural land surfaces, solar radiation becomes the only source of energy controlling most micrometeorological events in the layer of soil. This energy is used for heating up of air, evaporation and soil heating. The fundamental equation for estimating the surface energy components at the ground surface is based on the law of conservation of energy (Garcia and Sergio, 2005):

$$\Delta E = R - (G + LE + H) \tag{3.1}$$

where $\Delta E$ denotes the change in energy, $R$ is net radiation (Wm$^{-2}$), $G$ is ground heat flux (Wm$^{-2}$), $H$ is sensible heat flux (Wm$^{-2}$) and $LE$ is latent heat flux (Wm$^{-2}$). On globally averaged scale $\Delta E = 0$, which represent the planetary energy balance and hence equation (3.1) can be written as:

$$R = G + LE + H \tag{3.2}$$

Sensible heat flux is the amount of heat energy transferred from the Earth's surface to the atmosphere by conduction and convection due to the temperature difference between them. Heat is initially transferred into the air by conduction as air molecules collide with those of the surface. As air warms, it circulates upwards via convection. Thus the transfer of $H$ is accomplished in a two step process. Because air is such a poor conductor of heat, it is convection that is the most efficient way of transferring heat into the air.

When the surface is warmer than the air above, heat will be transferred upwards into the air as a positive sensible heat transfer. The transfer of heat raises the air's temperature but cools the surface. If air is warmer than the surface, heat is transferred from the air to the surface creating a negative sensible heat transfer. If heat is transferred out of the air, the air cools and the surface warms. This situation may take place at night when the Sun goes down and there is no input of solar radiation. Sensible heat flux is formulated in terms of the difference between surface temperature $(T_s)$ and air temperature $(T_a)$ according to equation 2.2.

## 3.4 Remote sensing in the thermal infrared

### 3.4.1 Thermal radiation

Each body emits electromagnetic radiation depending on its temperature and in general, any hot object (by which in this context, one which is not at absolute zero) will distribute its emission over a range of wavelengths and directions due to kinetic energy of molecules within the body. Measurements of the thermal radiation thus provide an important method for remote sensing that does not require instruments to be in close contact to the measured object.

In order to describe the radiative characteristics of the Earth–atmosphere system, it is convenient to introduce the concept of a blackbody. A blackbody is an object that absorbs all incident electromagnetic energy. If the body is in thermal equilibrium with its environment at finite temperature, it will on average emit exactly as much radiation as it absorbs, at every wavelength. At room temperature, black bodies emit infrared light and start emitting at visible wavelength as the temperature increases above a few hundred degrees Celsius (Kabsch, 2009). The amount of black body spectral radiance at a given wavelength and temperature is described by Planck's black–body radiation law:

$$B_{\lambda,T} = \frac{2hC^2\lambda^{-5}}{\exp\left(\frac{hC}{\lambda kT}\right) - 1} \tag{3.5}$$

where $B_{\lambda,T}$ is the spectral emittance of a blackbody ($\mathrm{Wm^{-2}\mu m^{-1}sr^{-1}}$), $T$ is the object temperature (K), $h = 6.626068\times10^{-34}$ is the Planck's constant (Js), $k = 1.38066\times10^{-23}$ is the Boltzmann constant ($\mathrm{JK^{-1}}$) and $C = 2.997925\times10^{10}$ is the velocity of light in a vacuum ($\mathrm{cms^{-1}}$). The constants are grouped together to form the first and second radiation constants: $C_1$ and $C_2$: $C_1 = 2hC^2$ ($\mathrm{Wcm^2\ Sr^{-1}}$) or $C_1 = 2\pi hC^2$ ($\mathrm{Wcm^2}$) and $C_2 = \frac{hC}{k}$ cm $K$. Hence equation (3.5) becomes:

$$B_{\lambda,T} = \frac{C_1\lambda^{-5}}{\exp\left(C_2/\lambda T\right) - 1} \tag{3.6}$$

The precise formula for the Planck function depends on whether the radiance is reckoned as "per unit frequency'', "per unit wavelength" or "per unit wave number" basis. This work reckons the Planck's function in terms of wave number ($\upsilon$): Writing in terms of $\upsilon$, where $\upsilon = \lambda^{-1}$ and $d\lambda = \frac{-d\upsilon}{\upsilon^2}$ we have:

$$B_{\upsilon,T} = \frac{C_1\upsilon^3}{\exp\left(C_2\upsilon / T\right)-1} \tag{3.7}$$

Assuming there are no atmospheric effects in the process of transferring emitted spectral radiance from the surface through the atmosphere to the sensor and given a Lambertian surface, the temperature of the ground object, so called brightness temperature $(T_b)$, can be determined by measuring the emitted spectral radiance, $B_{\upsilon,T}$ and inverting the Planck's function at a fixed wave number yielding:

$$T_b = \frac{C_2\upsilon}{\ln\left[\frac{C_1\upsilon^3}{B_{\upsilon,T}}+1\right]} \tag{3.8}$$

Real objects do not absorb all incident radiation and thus have lower thermal emission than a black body. This motivates the definition of emissivity: ratio of spectral radiance actually emitted by an object at some temperature and the radiance emitted by a black body at the same temperature (Sobrino *et al.*, 2008):

$$\varepsilon_{\lambda,\theta} = \frac{I_{\lambda,\theta}(T)}{B_{\lambda,\theta}(T)} \qquad 0 < \varepsilon_{\lambda,\theta} < 1 \tag{3.9}$$

All natural surfaces are characterized by emissivity less than unity, with the absolute value depending on factors such as temperature $(T)$, emission angle $(\theta)$ and wavelength $(\lambda)$. If the last dependency is only moderate within a range of wavelengths, the emissivity of the object can be approximated by a constant (grey body). The spectral emissivity $(\varepsilon_{\lambda,\theta})$ is related to the spectral reflectivity $(\rho_{\lambda,\theta})$ according to:

$$\varepsilon_{\lambda,\theta} = 1 - \rho_{\lambda,\theta} \qquad (3.10)$$

and hence a body or a surface with an emissivity not equal to unity will reflect part of the energy radiated onto it.

Atmospheric transmittance $(\tau_{\upsilon})$ is a critical parameter that affects the accuracy of sensible heat flux estimated. It depicts the magnitude of attenuation of thermal radiance transferring through the atmosphere. Radiance characterizes total emission. It indicates how much power emitted by an emitting surface is received by the sensor looking at some geometry. It is affected by a range of atmospheric constituents, including water vapour, carbon dioxide, ozone, methane and carbon monoxide in the order of decreasing importance. Comparing the magnitude of their effects, water vapour is the most abundant factor influencing the radiance transfer in the thermal spectral range. A related term is absorptance which is the fraction of radiance absorbed by a sample at a specified wavelength. Transmittance $(\tau_{\upsilon})$ and absorptance $(a_{\upsilon})$ are related by a mathematical expression:

$$a_{\upsilon} = 1 - \tau_{\upsilon} \qquad (3.11)$$

### 3.4.2 Radiative transfer theory

Electromagnetic radiation transports energy that is quantifiable in terms of spectral radiance ($Wm^{-2}\mu m^{-1}Sr^{-1}$). While travelling from the surface to the sensor, electromagnetic energy may be absorbed and scattered by the various atmospheric gases and aerosols with atmospheric water vapor being the main agent of these effects in the thermal infrared. The atmosphere emits radiation as a function of its own temperature profile and wavelength. From foregoing Planck's law of radiation, emitted radiation is a function of both $T$ and $\lambda$ and hence for a constant temperature, maximum amount of radiation is emitted at a particular wavelength, $\lambda_m$.

At long wavelengths, i.e., for microwaves and thermal infrared radiation, it is the emitted radiation and not reflected solar radiation that is important. The three emitted thermal components considered here arise from three categories: surface emitted radiation from the Earth $(L_1)$, downward, surface–reflected radiation from the atmosphere $(L_2)$ and path–emitted radiance $(L_3)$. They are separately illustrated in Figure 3.2.

#### 3.4.2.1 Surface–emitted component

The primary source of energy for thermal imaging is the Earth itself. Different materials on the Earth, however, can emit different amounts of thermal energy even if they are at the same temperature. Most materials are not ideal blackbodies with 100% radiative efficiency. The efficiency with which real materials emit thermal radiation at different wavelength is determined by their emissivity $\varepsilon_\upsilon$. The emitted radiance at the Earth surface is therefore given by the expression:

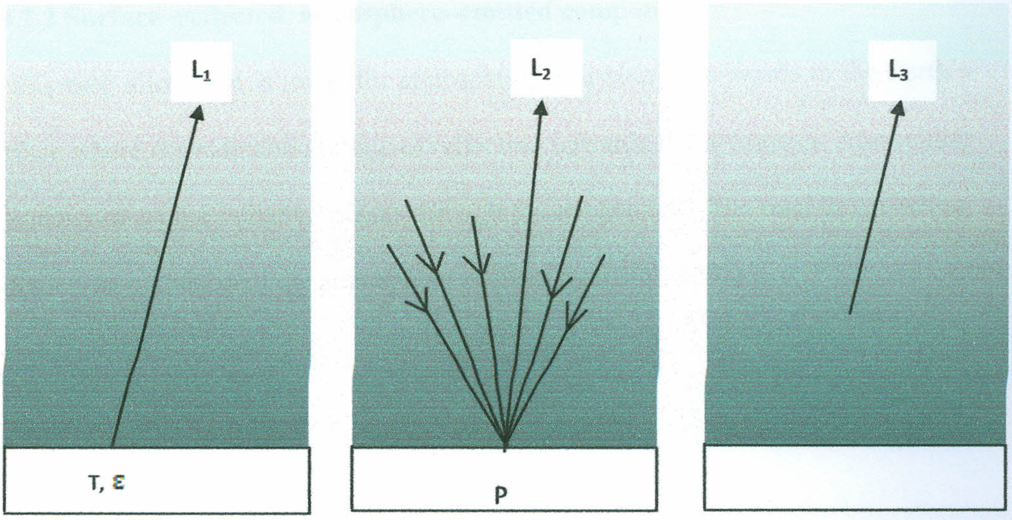

**Figure 3.2: The three emitted components in the IR region (8 to 15 μm).The shading in the diagram portray the decreasing atmospheric intensity at higher altitudes, (Schowengerdt, 2007).**

$$\varepsilon_{\upsilon} B_{\upsilon}(T_S) \tag{3.12}$$

The radiation emitted from the Earth's surface is transmitted by the atmosphere along the view path to the sensor. Hence, the radiance reaching the sensor from the terrestrial surface is given by:

$$L_1 = \varepsilon_{\upsilon} \tau_{\upsilon} B_{\upsilon}(T_S) \tag{3.13}$$

where $\tau_{\upsilon}$ is the total atmospheric spectral transmittance for wave number $\upsilon$ between the surface and the sensor.

### 3.4.2.2 Surface–reflected, atmosphere–emitted component

In this case allowance is made for atmospheric emission downwards to the Earth's surface where the radiation undergoes reflection upwards to the scanner. Attenuation is undergone as the radiation passes through the atmosphere. The total downwelling radiation from the top of the atmosphere is given by (Mito, 2002):

$$\tau_{\upsilon} \int_{\tau_{\upsilon}}^{1} B(T(p))/\tau_{\upsilon}(p) d\tau_{\upsilon}(p) \qquad (3.14$$

On reaching the Earth surface, a fraction $(1-\varepsilon_{\upsilon})$ of this is reflected at the Earth's surface and a fraction $\tau_{\upsilon}$ of this passes through the atmosphere so that the radiance reaching the satellite is given by:

$$L_2 = (1-\varepsilon_{\upsilon})\tau_{\upsilon}^2 \int_{\tau_{\upsilon}}^{1} B_{\upsilon}(T(p))/\tau_{\upsilon}^2(p) d\tau_{\upsilon}(p) \qquad (3.15)$$

### 3.4.2.3 Path–emitted component

The atmosphere also emits radiation upward as a function of temperature at different attitudes. The total energy that arrives at the sensor is integrated over the view path from the contribution at all altitudes. As the emitted radiation travels upwards to the scanner, it undergoes attenuation in the overlying atmosphere.

The formulation of path–emitted component, for a discrete layered atmosphere, is similar to that for the surface contribution except that appropriate layer emissivity $(\varepsilon_{\upsilon}^{l})$, Planck function at layer temperature $B_{\upsilon}(T_l)$ and vertical transmittance $\tau_p$

would be used. The contribution for all atmospheric layers is then given by the expression:

$$\sum_{layers} \varepsilon_{\upsilon}^{l} B_{\upsilon}(T_l)\tau_p(layer \rightarrow Top) \tag{3.16}$$

For an infinitely layered atmosphere and assuming local thermodynamic equilibrium, then the upwelling emitted radiation received at the satellite can thus be written as (Mito, 2002):

$$L_3 = \int_{\tau_\upsilon}^{1} B(T(p))d\tau_\upsilon(p) \tag{3.17}$$

where $T(p)$ is the temperature at the height at which the pressure is $p$ and $\tau_\upsilon(p)$ is the spectral transmittance from any pressure level $p$ to the top of the atmosphere.

Therefore on the condition of local thermodynamic equilibrium in clear sky, assuming the Earth's surface is Lambertian, and that the atmosphere is non–scattering, then from equations (3.13), (3.15) and (3.17), the radiative transfer equation for the sensor received radiance (watt cm$^{-2}$ sr$^{-1}$µm$^{-1}$) on board the satellite at any selected radiometric band centered in $\upsilon$ is given by:

$$I_\upsilon = \varepsilon_\upsilon \tau_\upsilon B_\upsilon(T_s) + (1-\varepsilon_\upsilon)\tau_\upsilon^2 \int_{\tau_\upsilon}^{1} B_\upsilon(T(p))/\tau_\upsilon^2(p)d\tau_\upsilon(p) + \int_{\tau_\upsilon}^{1} B(T(p))d\tau_\upsilon(p) \tag{3.18}$$

For the sake of convenience upwelling and downwelling emission can be defined respectively as (Ulivieri, 1984):

$$\overline{B}_{\upsilon} = \frac{\int_{\tau_{\upsilon}}^{1} B_{\upsilon}(T(p))\,d\tau_{\upsilon}(p)}{\int_{\tau_{\upsilon}}^{1} d\tau_{\upsilon}(p)} \tag{3.19}$$

$$\overline{\overline{B}}_{\upsilon} = \frac{\int_{\tau_{\upsilon}}^{1} \frac{B_{\upsilon}(T(p))}{\tau_{\upsilon}^{2}(p)}\,d\tau_{\upsilon}(p)}{\int_{\tau_{\upsilon}}^{1} \frac{d\tau_{\upsilon}(p)}{\tau_{\upsilon}^{2}(p)}} \tag{3.20}$$

where $\overline{B\upsilon}$ is the upwelling atmospheric mean radiance emitted upwards by the atmospheric layer between land surface and the sensor, $\overline{\overline{B}}_{\upsilon}$ is the downwelling atmospheric mean radiance that contributes, after reflection, to the signal measured by the sensor.

It is worth noting that from equations (3.18), (3.19) and (3.20), $I_{\upsilon}$ may also be expressed in terms of channel–equivalent quantities; namely $\varepsilon_{\upsilon}$, $\tau_{\upsilon}$, $\overline{B\upsilon}$ and $\overline{\overline{B}}_{\upsilon}$ as:

$$I_{\upsilon} = \varepsilon_{\upsilon} B_{\upsilon}(T_{s})\tau_{\upsilon} + \overline{B}\upsilon(1-\tau_{\upsilon}) + (1-\varepsilon_{\upsilon})(1-\tau_{\upsilon})\tau_{\upsilon}\overline{\overline{B}}\upsilon \tag{3.21}$$

The first term on the right hand side of equation (3.21) represents the contribution of terrestrial surface reduced by atmospheric absorption along the upward path; the second term represents the path–radiance, atmospheric contribution in upward direction, which depends on water vapor and temperature profiles. The third term represents the downward radiation $\overline{\overline{B}}\upsilon$ emitted by the atmosphere, reaches the Earth surface and is reflected by the ground $(1-\varepsilon_{\upsilon})$ towards the sensor with attenuation of the atmosphere $\tau_{\upsilon}$ along the upward path.

### 3.5 The surface temperature equation

Introducing the quantities $E_{\upsilon}$ and $A_{\upsilon}$ to equation (3.21), we have:

$$\begin{cases} E_{\upsilon}=\varepsilon_{\upsilon}\tau_{\upsilon} \\ A_{\upsilon}=(1-\tau_{\upsilon})\left[1+(1-\varepsilon_{\upsilon})\tau_{\upsilon}z_{\upsilon}\right] \end{cases} \tag{3.22}$$

where

$$z_{\upsilon}=\frac{\overline{\overline{B}}_{\upsilon}}{\overline{B}_{\upsilon}} \tag{3.23}$$

From equations (3.21), (3.22) and (3.23), the radiative transfer equation for the total radiance emerging at the top of a non–scattering cloud–free atmosphere is given by the relationship:

$$I_{\upsilon}=E_{\upsilon}B_{\upsilon}(T_{s})+A_{\upsilon}\overline{B}_{\upsilon} \tag{3.24}$$

The formulation of the GSWT, for retrieval of LST, is based on a suitable combination of the relations derived from equation (3.24) for two adjacent spectral channels: (Mito *et al*., 2006)

$$\begin{cases} I_{31}=E_{31}B_{31}(T_s)+A_{31}\overline{B}_{31} \\ I_{32}=E_{32}B_{32}(T_s)+A_{32}\overline{B}_{32} \end{cases} \tag{3.25}$$

This may be achieved by expanding equation (3.25) around a reference temperature. According to McMillin (1975, 1980), it is considerably more accurate, especially when the wavelengths are close to each other, to expand the Planck's function at a reference wavelengths. Adapting McMillin's results to the formalism of equation (3.25), the following system of equations is found:

$$\begin{cases} I_{31}=E_{31}B_{31}(T_s)+A_{31}B_{31}(\overline{T}_{31}) \\ B_{31}(T_{32})=B_{31}(T_s)E_{32}(1-\alpha)+B_{31}(\overline{T}_{32})A_{32} \end{cases} \tag{3.26}$$

where subscripts 31 and 32 indicate the split window channels, centred at the lower (taken as reference) and higher wavelength. $\overline{T}_{31}$ and $\overline{T}_{32}$ are the atmospheric brightness temperatures in the two thermal channels, $T_{32}$ is the corresponding brightness temperature of $I_{32}$ while $\alpha$ is a shifting correcting term given by (Mito, 2002):

$$\alpha = \frac{1-\varepsilon_{32}}{\varepsilon_{32}}\tau_2\left[\frac{\upsilon_{31}}{\upsilon_{32}}\frac{\exp\left(\frac{C_2\upsilon_{31}}{T_{31}}\right)-\exp\left(\frac{C_2(\upsilon_{31}-\upsilon_{32})}{T_s}\right)}{\exp\left(\frac{C_2\upsilon_{31}}{T_s}\right)-1}\right] \tag{3.27}$$

where $C_2 = 1.43879$ (cm K) is the second radiation constant and $\upsilon_{31}$ and $\upsilon_{32}$ are the central wave numbers of MODIS channels 31 and 32, respectively.

Radiative transfer numerical simulations indicate that a mathematical relationship between $\overline{T}_{31}$ and $\overline{T}_{32}$ exist; namely (Ulivieri *et al.*, 1985):

$$B_{31}(T_a) - B_{31}(\overline{T}_{32}) = c\left(B_{31}(T_a) - B_{31}(\overline{T}_{31})\right) \tag{3.28}$$

where $c$ is a regression coefficient and $T_a$ is the standard 2m height air temperature. $B_{31}(T_i)$ $(i = a, 31, 32)$ are radiance corresponding to air temperature and the brightness temperatures; $\overline{T}_{31}$ and $\overline{T}_{32}$ respectively. They are better defined by extending formulations in equations (3.8) and (3.9) giving:

$$\begin{cases} B_{31}(T_a) = \dfrac{C_1 \upsilon_{31}^3}{\exp\left(\dfrac{C_2 \upsilon_{31}}{T_a}\right) - 1} \\ B_{31}(\overline{T}1) = \dfrac{C_1 \upsilon_{31}^3}{\exp\left(\dfrac{C_2 \upsilon_{31}}{\overline{T}31}\right) - 1} \\ B_{31}(\overline{T}2) = \dfrac{C_1 \upsilon_{31}^3}{\exp\left(\dfrac{C_2 \upsilon_{31}}{\overline{T}32}\right) - 1} \end{cases} \tag{3.29}$$

and

$$\begin{cases} \overline{T}31 = \dfrac{C_2 \upsilon_{31}}{\log\left(\dfrac{C_1 \upsilon_{31}^3}{\overline{B}31} + 1\right)} \\ \overline{T}32 = \dfrac{C_2 \upsilon_{32}}{\log\left(\dfrac{C_1 \upsilon_{32}^3}{\overline{B}31} + 1\right)} \end{cases} \tag{3.30}$$

where $B_{31}(\overline{T}31)$ and $B_{31}(\overline{T}32)$ are the mean upwelling radiances corresponding to MODIS bands 31 and 32 respectively.

Adding the quantities $B_{31}(T_s) - B_{31}(T_s)$ and $cB_{31}(T_s) - cB_{31}(T_s)$ to the left and right hand side of equation (3.28) respectively, we obtain:

$$B_{31}(T_s) - B_{31}(\overline{T}32) - c\big(B_{31}(T_s) - B_{31}(\overline{T}31)\big) = (1-c)\big(B_{31}(T_s) - B_{31}(\overline{T}a)\big) \tag{3.31}$$

From equations (3.25) and (3.31), the following system of equation results:

$$\begin{cases} B_{31}(\overline{T}31) = \dfrac{I_{31}}{A_{31}} - \dfrac{B_{31}(T_s)E_{31}}{A_{31}} \\ B_{31}(\overline{T}32) = \dfrac{B_{31}(T_{32})}{A_{32}} - \dfrac{B_{31}(T_s)E_{32}}{A_{32}} \\ B_{31}(T_s) - \dfrac{B_{31}(T_s)}{A_{32}} + \dfrac{B_{31}(T_s)E_{32}}{A_{32}} - c\left[B_{31}(T_s) - \dfrac{I_{31}}{A_{31}} + \dfrac{B_{31}(T_s)E_{31}}{A_{31}}\right] = \\ (1-c)\left[B_{31}(T_s) - B_{31}(T_a)\right] \end{cases} \tag{3.32}$$

Rearranging the third part of equation (3.32), we have:

$$B_{31}(T_s) = \frac{cA_{32}I_{31} - A_{31}B_{31}(T_{32}) + A_{31}A_{32}(c-1)\big(B_{31}(T_s) - B_{31}(\overline{T}a)\big)}{cA_{32}(A_{31}+E_{31}) - A_{31}(A_{32}+E_{32})} \tag{3.33}$$

By letting

$$D^* = cA_{32}(A_{31} + E_{31}) - A_{31}(A_{32} + E_{32}) \tag{3.34}$$

Equation (3.33) can be written as:

$$B_{31}(T_s) = \frac{cA_{32}I_{31}}{D*} - \frac{A_{31}B_{31}(T_{32})}{D*} + \frac{(c-1)A_{31}A_{32}\left(B_{31}(T_s) - B_{31}(\bar{T}a)\right)}{D*} \qquad (3.35)$$

Adding the quantity $A_{31}\frac{I_{31}}{D*} - A_{31}\frac{I_{31}}{D*}$ to the right hand side of equation (3.35) we have:

$$B_{31}(T_s) = I_{31}\left(\frac{cA_{32} - A_{31}}{D*}\right) + \frac{A_{31}}{D*}\left(I_{31} - B_{31}(T_{32})\right) + \frac{(c-1)A_{31}A_{32}}{D*}\left[B_{31}(T_s) - B_{31}(\bar{T}a)\right] \qquad (3.36)$$

Letting

$$\begin{cases} a_1 = \frac{(cA_{32} - A_{31})}{D*} \\ a_2 = \frac{A_{31}}{D*} \\ a_3 = \frac{(c-1)A_{32}A_{31}}{D*} \end{cases} \qquad (3.37\text{ a})$$

the following formula results:

$$B_{31}(T_s) = a_1 I_{31} + a_2\left(I_{31} - B_{31}(T_{32})\right) + a_3\left(B_{31}(T_s) - B_{31}(T_a)\right) \qquad (3.37\text{ b})$$

Adding and subtracting $I_{31}$ on the right hand side of equation (3.37b) we obtain the following generalized algorithm for retrieving $T_s$:

$$B_{31}(T_s) = I_{31} + (a_1 - 1)I_{31} + a_2\left(I_{31} - B_{31}(T_{32})\right) + a_3\left(B_{31}(T_s) - B_{31}(T_a)\right) \qquad (3.38)$$

Coefficients $a_1$, $a_2$ and $a_3$ are functions of the surface spectral emittance, atmospheric water vapour content and the temperature profile of the atmosphere. An estimate of the corrective contributions is performed if the linearised Planck's function around $T_{31}$ is used. Hence:

$$\begin{cases} B_{31}(T_s)=B_{31}(T_{31})+\left.\dfrac{\partial B_{31}(T_s)}{\partial T_s}\right|_{T_{31}}(T_s-T_{31}) \\ B_{31}(T_{32})=B_{31}(T_{31})+\left.\dfrac{\partial B_{31}(T_{32})}{\partial T_{32}}\right|_{T_{31}}(T_{32}-T_{31}) \\ B_{31}(T_a)=B_{31}(T_{31})+\left.\dfrac{\partial B_{31}(T_a)}{\partial T_a}\right|_{T_{31}}(T_a-T_{31}) \end{cases} \tag{3.39}$$

From equation (3.39), we have:

$$\begin{cases} B_{31}(T_s)=B_{31}(T_{31})+\dfrac{\partial B_{31}(T_{31})}{\partial T_{31}}(T_s-T_{31}) \\ B_{31}(T_{32})=B_{31}(T_{31})+\dfrac{\partial B_{31}(T_{31})}{\partial T_{31}}(T_{32}-T_{31}) \\ B_{31}(T_a)=B_{31}(T_{31})+\dfrac{\partial B_{31}(T_{31})}{\partial T_{31}}(T_a-T_{31}) \end{cases} \tag{3.40}$$

Let the radiance measured by channel $\upsilon$ be:

$$I_\upsilon = B_\upsilon(T_\upsilon) \tag{3.41}$$

Inserting equations (3.40) and (3.41) into (3.38) yields:

$$\begin{aligned}\frac{\partial B_{31}(T_{31})}{\partial T_{31}}(T_s - T_{31}) = (a_1 - 1)B_{31}(T_{31}) + a_2\frac{\partial B_{31}(T_{31})}{\partial T_{31}}(T_{31} - T_{32}) \\ + a_3\frac{\partial B_{31}(T_{31})}{\partial T_{31}}(T_s - T_a)\end{aligned} \tag{3.42}$$

The Planck's function can be approximated by a simple power function (Sun and Pinker, 2003):

$$B_\upsilon(T_\upsilon) \approx \alpha_\upsilon T_\upsilon^n \tag{3.43}$$

Parameters $\alpha_\upsilon$ and $n$ are constants obtained by least squares regression fit. They vary from channel to channel of a given sensor. Hence from equation (3.43):

$$n_1 = \frac{T_{31}}{B_{31}(T_{31})}\frac{\partial B_{31}(T_{31})}{\partial T_{31}} \tag{3.44}$$

By letting $\beta = \frac{1}{n_1}$ and substituting equation (3.44) into (3.42), we eventually get:

$$T_s = T_{31} + \beta(a_1 - 1)T_{31} + a_2(T_{31} - T_{32}) + a_3(T_s - T_a) \tag{3.45}$$

where $\beta$, which does not vary greatly over temperature and spectral ranges of interest, is a term resulting from linearization (Mito *et al.*, 2006). From equations (3.44) and recalling the Planck's function, equation (3.8), $\beta$ is given by:

$$\beta = \frac{T_{31}}{C_2 \upsilon_{31}} \frac{\exp\left(\frac{C_2 \upsilon_{31}}{T_{31}}\right) - 1}{\exp\left(\frac{C_2 \upsilon_{31}}{T_{31}}\right)} \tag{3.46}$$

### 3.6. Aerodynamic resistance

The transfer of heat and water vapour from an evaporating surface into the air above the canopy encounters aerodynamic resistance $(r)$. Aerodynamic resistance describes resistance from the vegetation upward and involves friction from air flowing over vegetative surfaces. Parametization of aerodynamic resistance to heat and water transfer have a significant impact on the accuracy of models used to estimate sensible heat flux. Based on Monin–Obukhov Similarity (MOS) theory, many authors have proposed different parametization to estimate aerodynamic resistances to heat transfer. According to this theory, the determination of aerodynamic resistance requires information on aerodynamic properties of the canopy surface and atmospheric stability. It can be expressed as:

$$r = \frac{1}{k^2 u}\left[\ln\left(\frac{z-d}{z_{om}}\right) - \Psi_m\right]\left[\ln\left(\frac{z-d}{z_{oh}}\right) - \Psi_h\right] \tag{3.47}$$

where $k$ is the von Karman constant (equal to 0.41), $u$ is the wind speed at the reference height $z$, $z_{om}$ is the roughness length for momentum transfer (m), $z_{oh}$ (m) is roughness length for heat transfer (m), $d$ (m) is the height at which wind speed becomes essentially zero in the plant canopy (m) while $\psi_h$ and $\psi_m$ are stability corrections for heat and momentum respectively.

Reasonable estimates of aerodynamic properties $d$, $z_{om}$ and $z_{oh}$ have been obtained with several relationships as long as the surface is uniformly covered and fairly flat. Data has shown that for a wide variety of vegetation, these terms can be estimated from plant height $h_c$ as follows (Kustas, 1989):

$$\begin{cases} d = \frac{2}{3} h_c \\ z_{om} = \frac{1}{8} h_c \\ z_{oh} = \frac{1}{80} h_c \end{cases} \tag{3.48}$$

However, over a heterogeneous surface, a constant fraction may not be appropriate, though the error incurred by not using the appropriate fraction of $z_{om}$ for the scalar roughness may not be significant.

### 3.6.1 Aerodynamic resistance for neutral conditions

Assuming that the stability conditions are measured to be nearly neutral $T_s \approx T_a$ i.e., where temperature, atmospheric pressure and wind velocity distributions follow nearly adiabatic conditions, then $\Psi_m = \Psi_h = 0$ and equation (3.47) becomes:

$$r_o = \frac{1}{k^2 u}\left[\ln\left(\frac{z-d}{z_{om}}\right)\right]\left[\ln\left(\frac{z-d}{z_{oh}}\right)\right] \tag{3.49}$$

where $r_o$ is aerodynamic resistance in neutral conditions. In such conditions, adjustment of wind speed data obtained from instruments placed at elevations other than the standard height of 2 m is done using a logarithmic wind speed profile:

$$u_2 = u_z . \frac{4.87}{\ln(67.8h_c - 5.42)} \tag{3.50}$$

where $u_2$ is wind speed at 2 m above ground surface (ms$^{-1}$) and $u_z$ is measured wind speed at $z$ m above the ground surface (ms$^{-1}$). Daily or hourly mean wind speeds are alternatively used for 24–hour or hourly computations.

An alternative, semi-empirical, equation of $r_o$ is used for greenhouse conditions characterized by low wind speed (<1 m s$^{-1}$):

$$r_o = 4.72 . \frac{\left[\ln\left(\frac{z_w - d}{z_{om}}\right)\right]^2}{k^2 u_2} \tag{3.51}$$

### 3.6.2 Aerodynamic resistance for stable and unstable conditions

For stable and unstable conditions various parametization, more specifically focusing on the parametization of $\psi_m$ and $\psi_h$, have been developed on the basis of MOS theory to estimate aerodynamic resistance (Liu *et al.*, 2007). Choudhury and Monteith, 1988 proposed an appropriate equation for $r$ in non–neutral conditions:

$$r = \frac{r_o}{(1+\eta)^p} \tag{3.52}$$

where $p$ assumes the following values for various stability conditions: $p = 0$, neutral; $p = 0.75$, unstable and $p = 2$, stable. The stability factor , $\eta$, is defined by :

$$\eta = 5(z-d)g\frac{(T_S - T_a)}{T_a u^2} \tag{3.53}$$

with $g$ being the acceleration due to gravity (9.8 ms$^{-2}$). When $\psi < -5$, then $\psi = -5$.

In this study simulation of atmospheric effects, using PcLnWin software, was based on the radiative transfer equation (3.21). The modified General Split Window Technique algorithm (GSWT) for retrieval of LST was developed from the fundamental land surface temperature equation (3.45). Details of the data used, procedures followed in simulating atmospheric effects and the development of the modified GSWT are discussed in the next chapter.

# CHAPTER 4

# METHODOLOGY

## 4.1 Introduction

This chapter gives a description of PcLnWin software used in simulations. Characteristics of data used are outlined: including MODIS wavelength and filter functions, ground data and standard–built in atmospheric profiles. Procedures for simulating atmospheric effects including upwelling and downwelling atmospheric mean radiances are discussed. Also outlined are the steps followed in developing the modified GSWT for retrieval of surface temperature.

## 4.2 Description of software used

PcLnWin radiative transfer software version 3.0 from Ontar Corporation was used in simulating atmospheric effects (http://www.ontar.com). The software was used to simulate atmospheric transmittance and radiance for each of the atmospheric profiles used. PcLnWin consists of several distinct pieces; HIgh–resolution TRANsmission molecular absorption (HITRAN) database, Fast Atmospheric Signature Code (FASCODE) and line file generator.

The HITRAN database contains spectroscopic information on spectroscopic transitions of molecules through the infrared, visible and UV spectral regions (0–50000 cm$^{-1}$). FASCODE is a model and a computer program developed for accelerated computation of atmospheric radiance and spectral transmittance using line by line method for very high spectral resolution. Line file generator is a program used to search the HITRAN or user supplied line–by–line databases and allows one to limit the searches through the database based on spectral region, molecule type and temperature. In order to make complete simulations of atmospheric effects, several distinct steps were followed. They include: building line file, creating FASCODE input files and running FASCODE.

### 4.2.1 Building line file

For enhancement of good and fast performance of FASCODE run, a line file of spectral range 800 – 950 $cm^{-1}$ with three molecules ($H_2O$, $CO_2$ and $O_3$) was built from HITRAN database. The line file contains all the spectroscopic line data that FASCODE uses to compute transmittance and radiance.

### 4.2.2 FASCODE input files

PcLnWin provides a user interface program which organizes FASCODE inputs into logical screens called input cards, displaying only the variables relevant to the case one is setting up and provides consistency in input. The most commonly used cards in this work include cards 1.1 and 1.2, 1.3, 1.4, 3.1, 3.2, 3.4, 10.1 and 10.3. They are briefly described below:

In using PcLnWin software for simulating atmospheric effects, card 1.1 and 1.2 was used to set the calculation type, radiance and transmittance and to control major options that determine how FASCODE makes calculations. Through card 1.3, the spectral band (800–950 $cm^{-1}$) was set. Card 1.4 allowed boundary temperature, reflectivity and emissivity to be set, as explained in section 4.4. Card 3.1 allowed the selection of the model atmosphere. Details of atmospheres selected are discussed in section 4.3. By using card 3.2, the path geometry (including observer height, final height and zenith angle) were outlined. The path geometry was varied depending on the atmospheric effect being simulated. Through card 3.4, the number of atmospheric profile boundaries for a user defined atmosphere was specified. A total of 17 boundaries were defined by the software and each of them was accessed through card 3.5. The configuration of filters used for both MODIS bands 31 and 32 was done through card 10.1, while access to individual values of this filter was done through card 10.3.

### 4.2.3 FASCODE mode

After successfully creating FASCODE input files, FASCODE was run to compute integrated transmission and integrated emission for the spectral band pass and conditions specified in the study. The integrated transmission and emission for each of the profile and band were recorded in tape 6 output file.

### 4.2.4 FASCODE filter function and outputs

Another important part of FASCODE is the FASCODE filter function and FASCODE outputs. Access to the filter function was controlled by the variable, number of filter function, located on screen 1.1. Filters were defined by filling out the inputs on screen 10.1 and 10.3, specified by explicitly entering a table of values. FASCODE requires start wave number, end wave number and an increment between filter values. Table 4.1 shows a summary of such information, for both MODIS bands 31 and 32, used in the study.

Tape 6 is an important output file that contains information about FASCODE calculation just ended. The results of FASCODE run are stored in this output file. It

**Table 4.1: Start wave number, end wave number, increment between filter values and number of filter values for MODIS bands 31 and 32**

| | MODIS band 31 | MODIS band 32 |
|---|---|---|
| Start wave number | 866.60901 | 803.92102 |
| End wave number | 948.18500 | 858.65698 |
| Wave number increment | 1.8540 | 1.2440 |
| Number of filter values | 45 | 45 |

gives a summary of input screen, model atmosphere profiles and geometry calculation notes. This file is created by FASCODE as it runs. It allows the retrieval of integrated emission, integrated transmission and normalization factor of the filter.

### 4.3 General description of the data

Data used can be classified into three groups: MODIS wavelength and filter functions, user–defined atmospheric profiles and standard built–in atmospheric profiles.

#### 4.3.1 MODIS wavelength and filter functions

MODIS bands 31 and 32 centered at 11.03 μm and 12.02 μm and their filter functions were used in simulation. According to Wien's displacement law:

$$T\lambda_{\max} = 2897.9K\mu m \tag{4.1}$$

where $T$ is the temperature of the body and $\lambda_{\max}$ is the maximum wavelength.

This implies that for the Earth with a typical surface temperature of 300 K, the peak occurs at 9.6 μm. But the influence of ozone is felt at this wavelength and because of this; the 10 μm–12 μm range is commonly used for remote sensing. The wavelength locations for MODIS bands 31 and 32 are located in the same spectral range (Figure 1.1).

The filter functions of a particular sensor characterize the response of a sensor to available radiance in a particular wavelength range, at small discrete steps. It allows one to simulate what a lower spectral resolution instrument (imager or radiometer) can measure. The filter function includes the specification of initial filter value, wave number increment, number of filter values (Table 4.1) and specification of individual filters. Tables 4.2 a and 4.2 b shows filter values for MODIS bands 31 and 32 respectively used in simulating atmospheric effects in this work.

**Table 4.2 a: MODIS band 31 filter specifications**

<table>
<tr><td colspan="2">Start wave number<br>866.609</td><td>Wave number increment<br>1.854</td><td colspan="2">Number of Filter Values<br>45</td></tr>
<tr><td colspan="5">FILTER SPECIFICATION</td></tr>
<tr><td>0.000113</td><td>0.000171</td><td>0.000273</td><td>0.000426</td><td>0.000697</td></tr>
<tr><td>0.001077</td><td>0.001596</td><td>0.002277</td><td>0.003149</td><td>0.004121</td></tr>
<tr><td>0.005172</td><td>0.006288</td><td>0.00734</td><td>0.008257</td><td>0.008969</td></tr>
<tr><td>0.009525</td><td>0.009905</td><td>0.010245</td><td>0.010475</td><td>0.010846</td></tr>
<tr><td>0.011242</td><td>0.011708</td><td>0.011986</td><td>0.012163</td><td>0.01224</td></tr>
<tr><td>0.012051</td><td>0.011912</td><td>0.011851</td><td>0.011609</td><td>0.011416</td></tr>
<tr><td>0.010872</td><td>0.010033</td><td>0.008952</td><td>0.007617</td><td>0.006208</td></tr>
<tr><td>0.004777</td><td>0.003507</td><td>0.002478</td><td>0.001638</td><td>0.001019</td></tr>
<tr><td>0.000629</td><td>0.000379</td><td>0.000241</td><td>0.000149</td><td>0.0000439</td></tr>
</table>

Table 4.2 b: MODIS band 32 filter specifications

<table>
<tr><td colspan="2">Initial Filter Value<br>803.921</td><td colspan="2">Wave number increment<br>1.244</td><td>Number of Filter Values<br>45</td></tr>
<tr><td colspan="5">FILTER SPECIFICATION</td></tr>
<tr><td>0.000162</td><td>0.00024</td><td>0.00045</td><td>0.000885</td><td>0.001691</td></tr>
<tr><td>0.003194</td><td>0.005598</td><td>0.008575</td><td>0.011353</td><td>0.013297</td></tr>
<tr><td>0.014425</td><td>0.015171</td><td>0.01532</td><td>0.015184</td><td>0.015173</td></tr>
<tr><td>0.015283</td><td>0.015481</td><td>0.015596</td><td>0.015603</td><td>0.015785</td></tr>
<tr><td>0.016066</td><td>0.016431</td><td>0.016921</td><td>0.017329</td><td>0.017624</td></tr>
<tr><td>0.017839</td><td>0.017945</td><td>0.018018</td><td>0.018131</td><td>0.018253</td></tr>
<tr><td>0.018216</td><td>0.018017</td><td>0.017695</td><td>0.017161</td><td>0.015713</td></tr>
<tr><td>0.013148</td><td>0.01004</td><td>0.006901</td><td>0.004261</td><td>0.002483</td></tr>
<tr><td>0.001392</td><td>0.000772</td><td>0.000451</td><td>0.000271</td><td>0.000164</td></tr>
</table>

### 4.3.2. User–defined profiles

Twenty one atmospheric profiles obtained by periodic radiosounding (once a week), from Broglio Space Center (BSC) in Malindi, Kenya (Longitude: 40 degrees East, Latitude: 3 degrees South) were used. Each radiosounding contains the atmospheric profiles of temperature, pressure and concentration (in grams/cm$^2$/km) of water vapour ($H_2O$), carbon dioxide ($CO_2$), carbon monoxide (CO), ozone ($O_3$), and methane ($CH_4$), among other gases up to a maximum height of 40 km.

### 4.3.3. Standard built–in profiles

The standard built–in profiles used were: 1976 US Standard Atmosphere, Tropical Model, Midlatitude Summer, Midlatitude Winter, Subarctic Summer and Subarctic Winter. These profiles represent good average conditions, although the actual conditions of any given day can be significantly different, due to local weather. Each

By setting the sensor to "up looking" at an altitude of zero km, the atmospheric radiance emitted on the path to the instrument can be neglected. Under this assumption, the radiance measured by the near ground IR sensor consists solely of surface leaving radiance, namely radiance emitted by the surface and that reflected by the surface. At wave number $\upsilon$ the radiance emitted by the surface is approximated by the black body radiance $(B_{\upsilon})$ at the surface temperature $(T_S)$ of the surface multiplied by the emissivity $(\varepsilon_{\upsilon})$ of the surface. The radiance reflected by the surface is the product of absorptance $(1-\tau_{\upsilon})$, reflectance $(1-\varepsilon_{\upsilon})$ and downwelling atmospheric mean radiance $(\overline{\overline{B}}\upsilon)$. The total radiance leaving the surface and received by the sensor is thus approximated by:

$$I_{\upsilon} = \varepsilon_{\upsilon} B_{\upsilon}(T_S) + (1-\varepsilon_{\upsilon})(1-\tau_{\upsilon})\overline{\overline{B}}\upsilon \qquad (4.2)$$

Setting both surface emissivity and boundary temperature to zero implies that the contribution of terrestrial surface $\varepsilon_{\upsilon} B_{\upsilon}(T_S)$, from equation (4.2), can be neglected and the reflectance assume unity. The downwelling atmospheric mean radiance is therefore given by:

$$\overline{\overline{B}}\upsilon = \frac{I_{\upsilon}}{1-\tau_{\upsilon}} \qquad (4.3)$$

### 4.4.2 Upwelling atmospheric mean radiance

This is the component of radiance, majorly emitted terrestrial, directed upward from the Earth's atmosphere and received by a sensor. In order to simulate upwelling atmospheric mean radiance, the sensor was set to "down looking" at an altitude of

100 km in the Quick FasWin card of the PcLnWin software. A typical sensor geometry displayed is shown in Figure 4.2. Surface emissivity and boundary temperature were set to unity and zero respectively in card 1.4 of the PcLnWin software.

Observer Height: 100.000

H2: 0.000

Zenith Angle: 180.000

Down Short Path

ATM: User Supplied ATM

Ext:No Aerosol Attenuation

Bandpass

800.00 950.00 cm^-1

12.500 10.526 um

**Figure 4.2: Simulation geometry for upwelling atmospheric mean radiance**

Setting the sensor to "down looking" at an altitude of 100 km implies that the radiance it receives is given by the Radiative Transfer Equation (3.21). By setting surface emissivity to unity, the reflected part becomes zero and the last term on the right hand side of equation (3.21) vanishes. In this case, the radiance received by the sensor is given by:

$$I_v = B_v(T_s)\tau_v + \overline{B}_v(1-\tau_v)$$

Setting boundary temperature to zero implies that the contribution of terrestrial surface, $B_\upsilon(T_s)\tau_\upsilon$ in equation (4.4) can be neglected. The upwelling atmospheric mean radiance $(\overline{B}_\upsilon)$ is therefore given by:

$$\overline{B}\upsilon = \frac{I_\upsilon}{1-\tau_\upsilon} \tag{4.5}$$

Simulation results of $\overline{\overline{B}}_\upsilon$ and $\overline{B\upsilon}$, for the atmospheric profiles considered, are given in Table 5.4 and thereafter discussed.

### 4.5 Surface temperature retrieval

After an intensive review of the literature and the analysis of the problem to be solved, a modified form of the General Split Window Technique (GSWT) algorithm proposed by Mito *et al.*, 2006 was found to be the most suitable for retrieval of LST. The algorithm whose concepts originates from Ulivieri *et al.*, 1994, initially applied to AVHRR channels 4 and 5, has proved to be very accurate compared to several others and takes atmospheric effects into account, in particular the water vapour column (WVC) amount and a non–unitary surface emissivity for MODIS bands 31 and 32.

In both Ulivieri *et al.*, 1994 and Mito *et al.*, 2006, $T_s$ has been assumed to be equal to $T_a$, for the sake of simplicity. However, this assumption negates the concept of the sensible heat flux as $H$ depends on the difference between the two temperatures, equation (2.2). In this work, this assumption is removed. If $\varepsilon_{31} - \varepsilon_{32} = \overline{\varepsilon} = 1$, the first corrective term of equation (3.45) is zero. Then $T_s'$, the resulting retrieved surface temperature, is given as:

$$T_s' = T_{31} + a_2'(T_{31} - T_{32}) + a_3'(T_s - T_a) \tag{4.6}$$

and the surface emittance effect can be evaluated by:

$$T_s - T_s' = \beta(a_1 - 1)T_{31} + (a_2 - a_2')(T_{31} - T_{32}) + (a_3 - a_3')(T_s - T_a) \tag{4.7}$$

From equations (4.6) and (4.7) the surface temperature equation is re–defined as:

$$T_s = T_{31} + a_2'(T_{31} - T_{32}) + \beta(a_1 - 1)T_{31} + (a_2 - a_2')(T_{31} - T_{32}) + a_3(T_s - T_a) \tag{4.8}$$

The term $\beta$, which does not vary greatly over temperature and spectral ranges of interest, results from linearization (Mito *et al.*, 2006). Given that $E_i' = \tau_i$ and $A_i' = 1 - \tau_i$ are the values of the quantities $E_i$ and $A_i$, for assumed emissivity of unity, then from equation (3.22) we have:

$$\begin{cases} A_{31} = (1 - \tau_{31})\left[1 + (1 - \varepsilon_{31})\tau_{31} z_{31}\right] \\ A_{32} = (1 - \tau_{32})\left[1 + (1 - \varepsilon_{32})\tau_{32} z_{32}\right] \end{cases} \tag{4.9}$$

$$\begin{cases} E_{31}=\varepsilon_{31}\tau_{31} \\ E_{32}=\varepsilon_{32}\tau_{32} \end{cases} \tag{4.10}$$

$$\begin{cases} E'_{31}=\tau_{31} \\ E'_{32}=\tau_{32} \end{cases} \tag{4.11}$$

$$\begin{cases} A'_{31}=1-\tau_{31} \\ A'_{32}=1-\tau_{32} \end{cases} \tag{4.12}$$

By defining $\delta\varepsilon = \varepsilon_{31} - \varepsilon_{32}$ and $\varepsilon_{31} + \varepsilon_{32} = 2\overline{\varepsilon}$, it results that:

$$\begin{cases} E_{31}=E'_{31}\overline{\varepsilon}+0.5\partial\varepsilon E'_{31} \\ E_{32}=E'_{32}\overline{\varepsilon}-0.5\partial\varepsilon E'_{32} \end{cases} \tag{4.13}$$

$$\begin{cases} A_{31}=A'_{31}+(1-\overline{\varepsilon})A'_{31}E'_{31}z_{31}-0.5\partial\varepsilon A'_{31}E'_{31}z_{31} \\ A_{32}=A'_{32}+(1-\overline{\varepsilon})A'_{32}E'_{32}z_{32}+0.5\partial\varepsilon A'_{32}E'_{32}z_{32} \end{cases} \tag{4.14}$$

Or

$$\begin{cases} A_{31}=1-E'_{31}+(1-\overline{\varepsilon})A'_{31}E'_{31}z_{31}-0.5\partial\varepsilon A'_{31}E'_{31}z_{31} \\ A_{32}=1-E'_{32}+(1-\overline{\varepsilon})A'_{32}E'_{32}z_{32}+0.5\partial\varepsilon A'_{32}E'_{32}z_{32} \end{cases} \tag{4.15}$$

From the definition of $D^* = cA_{32}(A_{31}+E_{31}) - A_{31}(A_{32}+E_{32})$ in equation 3.34, we have:

$$cA_{32} = cA'_{32} + (1-\overline{\varepsilon})cA'_{32}E'_{32}z_{32} + 0.5\partial\varepsilon cA'_{32}E'_{32}z_{32} \tag{4.16}$$

$$A_{31} + E_{31} = 1 - E'_{31} + (1-\overline{\varepsilon})A'_{31}E'_{31}z_{31} - 0.5\partial\varepsilon A'_{31}E'_{31}z_{31} + E'_{31}\overline{\varepsilon} + 0.5\partial\varepsilon E'_{31} \tag{4.17}$$

$$A_{32} + E_{32} = 1 - E'_{32} + (1-\overline{\varepsilon})A_{32}E'_{32}z_{32} + 0.5\partial\varepsilon A_{32}E'_{32}z_{32} + E'_{32}\overline{\varepsilon} - 0.5\partial\varepsilon E'_{32} \tag{4.18}$$

$$\begin{aligned}
&cA_{32}(A_{31} + E_{31}) = \\
&cA'_{32} - cA'_{32}E'_{31} + \overline{\varepsilon}cA'_{32}E'_{31} + (1-\overline{\varepsilon})\left(cA'_{31}A'_{32}E'_{31}z_{31} + cA'_{32}E'_{32}z_{32}\right) + \\
&0.5\partial\varepsilon\left(-cA'_{31}A'_{32}E'_{31}z_{31} + cA'_{32}E'_{31} + cA'_{32}E'_{32}z_{32}\right) + \\
&\left((1-\overline{\varepsilon})^2 - (0.5\delta\varepsilon)^2\right)\left(cA'_{31}A'_{32}E'_{31}E'_{32}z_{31}z_{32} - cA'_{32}E'_{31}E'_{32}z_{32}\right)
\end{aligned} \tag{4.19}$$

$$\begin{aligned}
&A_{31}(A_{32} + E_{32}) = \\
&A'_{31} - A'_{31}E'_{32} + \overline{\varepsilon}A'_{31}E'_{32} + (1-\overline{\varepsilon})\left(A'_{31}A'_{32}E'_{32}z_{32} + A'_{31}E'_{31}z_{31}\right) + \\
&0.5\partial\varepsilon\left(A'_{31}A'_{32}E'_{32}z_{32} - A'_{31}E'_{32} - A'_{31}E'_{31}z_{31}\right) + \\
&\left((1-\overline{\varepsilon})^2 - (0.5\delta\varepsilon)^2\right)\left(A'_{31}A'_{32}E'_{31}E'_{32}z_{31}z_{32} - A'_{31}E'_{31}E'_{32}z_{31}\right)
\end{aligned} \tag{4.20}$$

Combining equations (4.19) and (4.20) we have:

$$\begin{aligned}
D^* &= cA'_{32} - A'_{31} \\
&+ (1-\overline{\varepsilon})\left\{A'_{32}\left[E'_{32}z_{32} - E'_{31}(1 - A'_{31}z_{31})\right]c + A'_{31}\left[E'_{32}(1 - A'_{32}z_{32}) - E'_{31}z_{31}\right]\right\} \\
&+ 0.5\delta\varepsilon\left\{A'_{32}\left[E'_{32}z_{32} + E'_{31}(1 - A'_{31}z_{31})\right]c + A'_{31}\left[E'_{32}(1 - A'_{32}z_{32}) + E'_{31}z_{31}\right]\right\} \\
&+ \left((1-\overline{\varepsilon})^2 - (0.5\delta\varepsilon)^2\right)\left[A'_{32}E'_{31}E'_{32}z_{32}(A'_{31}z_{31} - 1)c + A'_{31}E'_{31}E'_{32}z_{31}(1 - A'_{32}z_{32})\right]
\end{aligned} \tag{4.21}$$

From equations (3.37a) and (4.7), the following expressions for the numerator components of the surface emittance effect results:

$$\begin{aligned}
&\beta(a_1-1)T_{31}= \\
&-(1-\overline{\varepsilon})\beta\left(A'_{32}E'_{31}(A'_{31}z_{31}-1)c+A'_{31}E'_{32}(1-A'_{32}z_{32})\right)T_{31}+ \\
&\delta\varepsilon\left\{0.5\beta\left[A'_{32}E'_{31}(A'_{31}z_{31}-1)c-A'_{31}E'_{32}(1-A'_{32}z_{32})\right]T_{31}\right\}- \\
&((1-\overline{\varepsilon})^2-(0.5\delta\varepsilon)^2)\beta\left\{E'_{31}E'_{32}\left[A'_{32}z_{32}(A'_{31}z_{31}-1)c+A'_{31}z_{31}(1-A'_{32}z_{32})\right]T_{31}\right\}
\end{aligned}\tag{4.22}$$

$$\begin{aligned}
&(a_2-a'_2)(T_{31}-T_{32})= \\
&-(1-\overline{\varepsilon})a'_2\left\{A'_{32}\left[E'_{32}z_{32}-E'_{31}(1+z_{31}E'_{31})\right]c+A'_{31}E'_{32}(1-A'_{32}z_{32})\right\}(T_{31}-T_{32})+ \\
&\delta\varepsilon 0.5a'_2\left\{A'_{32}\left(-E'_{32}z_{32}-E'_{31}(1+E'_{31}z_{31})\right)c-A'_{31}E'_{32}(1-A'_{32}z_{32})\right\}\ (T_{31}-T_{32})- \\
&\left((1-\overline{\varepsilon})^2-(0.5\delta\varepsilon)^2\right)a'_2\left\{E'_{31}E'_{32}\left[A'_{32}z_{32}\left(A'_{31}z_{31}-1\right)c+A'_{31}z_{31}\left(1-A'_{31}z_{31}\right)\right]\right\}\ (T_{31}-T_{32})
\end{aligned}\tag{4.23}$$

$$\begin{aligned}
&a_3(T_s-T_a)= \\
&A'_{31}A'_{32}(c-1)(T_s-T_a) \\
&+(1-\overline{\varepsilon})\left(cA'_{31}A'_{32}(E'_{32}z_{32}+E'_{31}z_{31})-A'_{31}A'_{32}(E'_{32}z_{32}+E'_{31}z_{31})\right)(T_s-T_a) \\
&+0.5\delta\varepsilon\left(cA'_{31}A'_{32}(E'_{32}z_{32}-E'_{31}z_{31})-A'_{31}A'_{32}(E'_{32}z_{32}-E'_{31}z_{31})\right)(T_s-T_a) \\
&+\left((1-\overline{\varepsilon})^2-(0.5\delta\varepsilon)^2\right)\left((c-1)A'_{31}A'_{32}E'_{31}E'_{32}z_{31}z_{32}\right)(T_s-T_a)
\end{aligned}\tag{4.24}$$

Considering both the numerator and the denominator of the surface emittance effect, and from equations (4.8), (4.22), (4.23) and (4.24), we have:

$$T_s=T_{31}+a'_2(T_{31}-T_{32})+F_1(1-\overline{\varepsilon})+F_2\delta\varepsilon+F_3\left((1-\overline{\varepsilon})^2-(0.5\delta\varepsilon)^2\right)+F_4(T_s-T_a)\tag{4.25}$$

where $F_1=\frac{G_1}{D^*}$, $F_2=\frac{G_2}{D^*}$, $F_3=\frac{G_3}{D^*}$, $F_4=\frac{G_4}{D^*}$

$$
\begin{aligned}
G_1 = & -\beta\Big(A'_{32}E'_{31}(A'_{31}z_{31}-1)c + A'_{31}E'_{32}(1-A'_{32}{}_{32})\Big)\,T_{31} \\
& - a'_2\Big\{A'_{32}\Big[E'_{32}z_{32}-E'_{31}(1+z_{31}E'_{31})\Big]c+A'_{31}E'_{32}(1-A'_{32}z_{32})\Big\}(T_{31}-T_{32})
\end{aligned}
\tag{4.26}
$$

$$
\begin{aligned}
G_2 = & \, 0.5\Big\{\beta\Big(A'_{32}E'_{31}(A'_{31}z_{31}-1)c-A'_{31}E'_{32}(1-A'_{32}z_{32})\Big)T_{31} \\
& +a'_2\Big[A'_{32}(-E'_{32}z_{32}-E'_{31}(1+z_{31}E'_{31}))c-A'_{31}E'_{32}(1-A'_{32}z_{32})\Big](T_{31}-T_{32})\Big\}
\end{aligned}
\tag{4.27}
$$

$$
\begin{aligned}
G_3 = & -\beta\Big\{E'_{31}E'_{32}\Big[A'_{32}z_{32}(A'_{31}z_{31}-1)c+A'_{31}z_{31}(1-A'_{32}z_{32})\Big]\Big\}T_{31} \\
& - a'_2\Big\{E'_{31}E'_{32}\Big[A'_{32}z_{32}(A'_{31}z_{31}-1)c+A'_{31}z_{31}(1-A'_{32}z_{32})\Big]\Big\}(T_{31}-T_{32})
\end{aligned}
\tag{4.28}
$$

$$
\begin{aligned}
G_4 = & \, A'_{31}A'_{32}(c-1) \\
& +(1-\bar{\varepsilon})\Big(cA'_{31}A'_{32}(E'_{32}z_{32}+E'_{31}z_{31})-A'_{31}A'_{32}(E'_{32}z_{32}+E'_{31}z_{31})\Big) \\
& +0.5\partial\varepsilon\Big(cA'_{31}A'_{32}(E'_{32}z_{32}-E'_{31}z_{31})-A'_{31}A'_{32}(E'_{32}z_{32}-E'_{31}z_{31})\Big) \\
& +\Big((1-\bar{\varepsilon})^2-(0.5\partial\varepsilon)^2\Big)\Big((c-1)A'_{31}A'_{32}E'_{31}E'_{32}z_{32}\Big)
\end{aligned}
\tag{4.29}
$$

Equation (4.25) is the modified General Split Window Technique (GSWT) algorithm used for retrieving LST. The functions $F_1$, $F_2$ and $F_3$ are analogous to $H_1$, $H_2$ and $H_3$ given by Mito *et al.*, 2006. They assumed that $T_s \approx T_a$ making it possible to eliminate $F_4$.

The results of radiances and the corresponding transmittances simulated, for each of the atmospheric profiles considered, were vital in evaluating downwelling and upwelling atmospheric mean radiances, according to equations (4.3) and (4.5) respectively. These results were then used to evaluate other atmospheric effects including brightness temperatures for MODIS bands 31 $(T_{31})$ and 32 $(T_{32})$, the ratio of downwelling to upwelling atmospheric mean radiance for both MODIS bands 31 $(z_{31})$ and 32 $(z_{32})$, the coefficients $a_i$ and $a_i^{'}$ (for assumed mean emissivities of 0.9 and 1 respectively) and the beta term according to formulations outlined in chapter three. The next chapter outlines the results of simulation of these atmospheric effects and the formulation of the proposed sensible heat flux algorithm.

# CHAPTER 5

# RESULTS AND DISCUSSIONS

## 5.1 Introduction

This chapter discusses the results of simulation of atmospheric effects used in the development of a general algorithm for estimating sensible heat flux. The assessment of the effects of different atmospheric stabilities is discussed. Also presented are the validation results of the proposed algorithm.

## 5.2 Results of simulation of atmospheric effects

The atmospheric effects considered include atmospheric water vapour, atmospheric radiance and transmittance, downwelling and upwelling atmospheric mean radiance, ratio of downwelling to upwelling atmospheric mean radiance, coefficients $a_i$ and $a_i^{'}$ (for assumed mean emissivities of 0.9 and 1 respectively), beta term and the brightness temperatures for MODIS bands 31 $(T_{31})$ and 32 $(T_{32})$.

### 5.2.1 Atmospheric water vapour

The absorption in the spectral region 10 μm–12 μm is mainly due to water vapour, carbon dioxide, ozone, methane and carbon monoxide in the order of decreasing importance. In this spectral range, water vapour is responsible for atmospheric effects with different intensity. Other gases absorb the radiance only in some selected parts of the spectral range, with the effect of ozone and carbon dioxide being almost constant (Figure 1.1). The concentration of water vapour in mol cm$^{-2}$ and g cm$^{-2}$ for each of the atmospheric profiles considered is shown in Table 5.1.

Table 5.1: Results of simulation of atmospheric water vapour

| Profile | Amount of water vapour (mol cm$^{-2}$) | Amount of water vapour (g cm$^{-2}$) |
|---|---|---|
| 01 (BSC. Malindi) | 1.806E+23 | 5.3973 |
| 02 (BSC. Malindi) | 1.394E+23 | 4.1660 |
| 03 (BSC. Malindi) | 9.557E+22 | 2.8562 |
| 04 (BSC. Malindi) | 1.399E+23 | 4.1810 |
| 05 (BSC. Malindi) | 1.387E+23 | 4.1451 |
| 06 (BSC. Malindi) | 1.374E+23 | 4.1063 |
| 07 (BSC. Malindi) | 1.000E+23 | 2.9885 |
| 08 (BSC. Malindi) | 1.407E+23 | 4.2049 |
| 09 (BSC. Malindi) | 9.943E+22 | 2.9715 |
| 10 (BSC. Malindi) | 1.614E+23 | 4.8235 |
| 11 (BSC. Malindi) | 1.250E+23 | 3.7357 |
| 12 (BSC. Malindi) | 1.196E+23 | 3.5743 |
| 13 (BSC. Malindi) | 1.430E+23 | 4.2736 |
| 14 (BSC. Malindi) | 1.584E+23 | 4.7339 |
| 15 (BSC. Malindi) | 1.601E+23 | 4.7847 |
| 16 (BSC. Malindi) | 1.038E+23 | 3.1021 |
| 17 (BSC. Malindi) | 1.483E+23 | 4.4320 |
| 18 (BSC. Malindi) | 1.092E+23 | 3.2635 |
| 19 (BSC. Malindi) | 1.238E+23 | 3.6998 |
| 20 (BSC. Malindi) | 1.157E+23 | 3.4577 |
| 21 (BSC. Malindi) | 1.425E+23 | 4.2587 |
| Tropical | 1.376E+23 | 4.1128 |
| Midlatitude summer | 9.776E+22 | 2.9220 |
| Mid latitude winter | 2.849E+22 | 0.8516 |
| Subarctic summer | 6.962E+22 | 2.0809 |
| Subarctic winter | 1.392E+22 | 0.4161 |
| US standard | 4.737E+22 | 1.4159 |

The concentration of water vapour simulated, in mol cm$^{-2}$, was converted to g cm$^{-2}$ using the conversion equation:

$$wv_2 = \frac{wv_1 \times n_2}{n_1} \tag{5.1}$$

where $wv_2$ is the concentration of water vapour (in g cm$^{-2}$), $wv_1$ is concentration of water vapour (in mol cm$^{-2}$), $n_2$ is the molar mass of water (18.0153 g mol$^{-1}$) and $n_1$ is the Avogadro's number ($6.02214179 \times 10^{23}$ mol$^{-1}$)

The results showed a wide range of atmospheric water vapour, from 0.4 g cm$^{-2}$ to 5.4 g cm$^{-2}$, which represents a wide range of atmospheres considered. Graphical analysis were carried to examine variations of different atmospheric effects with atmospheric water vapour and the results are shown in Figures 5.2, 5.3 and 5.4. This was fundamental in evaluating coefficients and regressive relationship required by the algorithm for estimating sensible heat flux.

### 5.2.2 Atmospheric transmittance and radiance

Simulation results of atmospheric transmittance and un–normalized radiance for two geometries of the sensor: "up looking" and "down looking" are shown in Tables 5.2 and 5.3 respectively. The radiances for bands 31 and 32 were normalized using normalization factors of 0.514603 and 0.621434 respectively. The normalized radiance and the corresponding transmittance were used in evaluating downwelling and upwelling atmospheric mean radiance, according to formulations in equations (4.3) and (4.5) respectively, and the results are shown in Table 5.4.

**Table 5.2: Results of simulation of atmospheric radiance and transmittance: sensor "up looking"**

| Profile | Band 31 | | Band 32 | |
|---|---|---|---|---|
| | Transmittance | Emittance $(Wcm^{-2}cm^{-1}sr^{-1})$ | Transmittance | Emittance $(Wcm^{-2}cm^{-1}sr^{-1})$ |
| 01 (BSC. Malindi) | 4.28801E-01 | 3.20560E-06 | 2.93191 E-01 | 5.41050E-06 |
| 02 (BSC. Malindi) | 5.68195 E-01 | 2.33749E-06 | 4.41772 E-01 | 4.12739E-06 |
| 03 (BSC. Malindi) | 6.76745 E-01 | 1.67244E-06 | 5.68048 E-01 | 3.05595E-06 |
| 04 (BSC. Malindi) | 5.30526 E-01 | 2.51390E-06 | 3.98615 E-01 | 4.39758E-06 |
| 05 (BSC. Malindi) | 5.27347 E-01 | 2.60610E-06 | 3.95473 E-01 | 4.53776E-06 |
| 06 (BSC. Malindi) | 5.26744 E-01 | 2.46011E-06 | 3.93919 E-01 | 4.30847E-06 |
| 07 (BSC. Malindi) | 6.90567 E-01 | 1.58789E-06 | 5.84979 E-01 | 2.91433E-06 |
| 08 (BSC. Malindi) | 5.59557 E-01 | 2.19692E-06 | 4.30082 E-01 | 3.90873E-06 |
| 09 (BSC. Malindi) | 6.95955 E-01 | 1.58107E-06 | 5.92622 E-01 | 2.89861E-06 |
| 10 (BSC. Malindi) | 5.19826 E-01 | 2.50703E-06 | 3.87190 E-01 | 4.38664E-06 |
| 11 (BSC. Malindi) | 5.93832 E-01 | 2.17986E-06 | 4.70186 E-01 | 3.88055E-06 |
| 12 (BSC. Malindi) | 6.37554 E-01 | 2.00631E-06 | 5.22858 E-01 | 3.59161E-06 |
| 13 (BSC. Malindi) | 5.06785 E-01 | 2.73372E-06 | 3.73175 E-01 | 4.73170E-06 |
| 14 (BSC. Malindi) | 4.87968 E-01 | 2.73279E-06 | 3.52519 E-01 | 4.72781E-06 |
| 15 (BSC. Malindi) | 5.11164 E-01 | 2.48510E-06 | 3.76353 E-01 | 4.34837E-06 |
| 16 (BSC. Malindi) | 7.11256 E-01 | 1.46768E-06 | 6.10972 E-01 | 2.70576E-06 |
| 17 (BSC. Malindi) | 5.18870 E-01 | 2.43040E-06 | 3.84915 E-01 | 4.26763E-06 |
| 18 (BSC. Malindi) | 6.81729 E-01 | 1.73032E-06 | 5.76870 E-01 | 3.13787E-06 |
| 19 (BSC. Malindi) | 5.97676 E-01 | 2.14115E-06 | 4.74371 E-01 | 3.81880E-06 |
| 20 (BSC. Malindi) | 5.96844 E-01 | 2.14423E-06 | 4.73107 E-01 | 3.82262E-06 |
| 21 (BSC. Malindi) | 5.93224 E-01 | 2.16808E-06 | 4.70748 E-01 | 3.85178E-06 |
| Tropical | 5.63912 E-01 | 2.35661E-06 | 4.36613 E-01 | 4.15411E-06 |
| Midlatitude summer | 7.14391 E-01 | 1.43624E-06 | 6.14279 E-01 | 2.65381E-06 |
| Midlatitude winter | 9.43093 E-01 | 1.93995E-07 | 9.16360 E-01 | 4.01725E-07 |
| Subarctic summer | 8.18612 E-01 | 7.91801E-07 | 7.45867 E-01 | 1.53328E-06 |
| Subarctic winter | 9.78701 E-01 | 5.96829E-08 | 9.66594 E-01 | 1.27774E-07 |
| US standard | 8.93005 E-01 | 4.41266E-07 | 8.48940 E-01 | 9.03303E-07 |

**Table 5.3: Results of simulation of atmospheric radiance and transmittance: sensor "down looking"**

| Profile | Band 31 | | Band 32 | |
|---|---|---|---|---|
| | Transmittance | Emittance $(Wcm^{-2}cm^{-1}sr^{-1})$ | Transmittance | Emittance $(Wcm^{-2}cm^{-1}sr^{-1})$ |
| 01 (BSC. Malindi) | 4.29295E-01 | 3.02474E-06 | 2.93191E-01 | 5.41050E-06 |
| 02 (BSC. Malindi) | 5.68032E-01 | 2.22908E-06 | 4.43141E-01 | 4.11437E-06 |
| 03 (BSC. Malindi) | 6.76743E-01 | 1.62937E-06 | 5.68048E-01 | 3.05595E-06 |
| 04 (BSC. Malindi) | 5.30525E-01 | 2.40689E-06 | 3.98615E-01 | 4.39758E-06 |
| 05 (BSC. Malindi) | 5.27345E-01 | 2.48381E-06 | 3.95473E-01 | 4.53776E-06 |
| 06 (BSC. Malindi) | 5.26673E-01 | 2.37450E-06 | 3.93919E-01 | 4.30847E-06 |
| 07 (BSC. Malindi) | 6.90563E-01 | 1.53166E-06 | 5.84979E-01 | 2.91433E-06 |
| 08 (BSC. Malindi) | 5.59555E-01 | 2.09094E-06 | 4.30082E-01 | 3.90873E-06 |
| 09 (BSC. Malindi) | 6.95953E-01 | 1.52789E-06 | 5.92622E-01 | 2.89861E-06 |
| 10 (BSC. Malindi) | 5.19823E-01 | 2.35707E-06 | 3.87190E-01 | 4.38664E-06 |
| 11 (BSC. Malindi) | 5.93829E-01 | 2.09510E-06 | 4.70186E-01 | 3.88055E-06 |
| 12 (BSC. Malindi) | 6.37548E-01 | 1.92494E-06 | 5.22858E-01 | 3.59161E-06 |
| 13 (BSC. Malindi) | 5.06801E-01 | 2.60861E-06 | 3.73175E-01 | 4.73170E-06 |
| 14 (BSC. Malindi) | 4.87961E-01 | 2.58789E-06 | 3.52519E-01 | 4.72781E-06 |
| 15 (BSC. Malindi) | 5.11164E-01 | 2.34960E-06 | 3.76353E-01 | 4.34837E-06 |
| 16 (BSC. Malindi) | 7.11252E-01 | 1.41401E-06 | 6.10972E-01 | 2.70576E-06 |
| 17 (BSC. Malindi) | 5.18740E-01 | 2.31687E-06 | 3.84915E-01 | 4.26763E-06 |
| 18 (BSC. Malindi) | 6.81723E-01 | 1.66198E-06 | 5.76870E-01 | 3.13787E-06 |
| 19 (BSC. Malindi) | 5.97675E-01 | 2.05616E-06 | 4.74371E-01 | 3.81880E-06 |
| 20 (BSC. Malindi) | 5.96844E-01 | 2.08017E-06 | 4.73107E-01 | 3.82262E-06 |
| 21 (BSC. Malindi) | 5.93278E-01 | 2.07411E-06 | 4.70748E-01 | 3.85178E-06 |
| Tropical | 5.64046E-01 | 2.25537E-06 | 4.36613E-01 | 4.15411E-06 |
| Midlatitude summer | 7.14410E-01 | 1.39082E-06 | 6.14279E-01 | 2.65381E-06 |
| Mid latitude winter | 9.43091E-01 | 1.90312E-07 | 9.16360E-01 | 4.01725E-07 |
| Subarctic Summer | 8.19026E-01 | 7.67034E-07 | 7.45867E-01 | 1.53328E-06 |
| Subarctic Winter | 9.78699E-01 | 5.90452E-08 | 9.66594E-01 | 1.27774E-07 |
| Us standard | 8.93005E-01 | 4.41266E-07 | 8.48940E-01 | 9.03303E-07 |

**Table 5.4: Results of evaluation of upwelling and downwelling atmospheric mean radiance**

| Profile | Upwelling atmospheric mean radiance ($Wcm^{-2}cm^{-1}sr^{-1}$) | | Downwelling atmospheric mean radiance ($Wcm^{-2}cm^{-1}sr^{-1}$) | |
|---|---|---|---|---|
| | Band 31 | Band 32 | Band 31 | Band 32 |
| 01 (BSC. Malindi) | 0.1030E-04 | 0.1143 E-04 | 0.1092E-04 | 0.1232E-04 |
| 02 (BSC. Malindi) | 0.1003E-04 | 0.1119 E-04 | 0.1052E-04 | 0.1189E-04 |
| 03 (BSC. Malindi) | 0.0979E-04 | 0.1102 E-04 | 0.1005E-04 | 0.1138E-04 |
| 04 (BSC. Malindi) | 0.0996E-04 | 0.1115 E-04 | 0.1041E-04 | 0.1177E-04 |
| 05 (BSC. Malindi) | 0.1021E-04 | 0.1138 E-04 | 0.1071E-04 | 0.1208E-04 |
| 06 (BSC. Malindi) | 0.0975E-04 | 0.1094 E-04 | 0.1010E-04 | 0.1144E-04 |
| 07 (BSC. Malindi) | 0.0962E-04 | 0.1081 E-04 | 0.0997E-04 | 0.1130E-04 |
| 08 (BSC. Malindi) | 0.0923E-04 | 0.1038 E-04 | 0.0969E-04 | 0.1104E-04 |
| 09 (BSC. Malindi) | 0.0977 E-04 | 0.1098 E-04 | 0.1011E-04 | 0.1145E-04 |
| 10 (BSC. Malindi) | 0.0954E-04 | 0.1066 E-04 | 0.1015E-04 | 0.1152E-04 |
| 11 (BSC. Malindi) | 0.1002E-04 | 0.1121 E-04 | 0.1043E-04 | 0.1179E-04 |
| 12 (BSC. Malindi) | 0.1032E-04 | 0.1152 E-04 | 0.1076E-04 | 0.1211E-04 |
| 13 (BSC. Malindi) | 0.1028E-04 | 0.1145 E-04 | 0.1077E-04 | 0.1215E-04 |
| 14 (BSC. Malindi) | 0.0982E-04 | 0.1096 E-04 | 0.1037E-04 | 0.1175E-04 |
| 15 (BSC. Malindi) | 0.0934 E-04 | 0.1046 E-04 | 0.0988E-04 | 0.1122E-04 |
| 16 (BSC. Malindi) | 0.0952E-04 | 0.1069 E-04 | 0.0988E-04 | 0.1119E-04 |
| 17 (BSC. Malindi) | 0.0936E-04 | 0.1050 E-04 | 0.0981E-04 | 0.1117E-04 |
| 18 (BSC. Malindi) | 0.1015E-04 | 0.1136 E-04 | 0.1056E-04 | 0.1193E-04 |
| 19 (BSC. Malindi) | 0.0993E-04 | 0.1114 E-04 | 0.1034E-04 | 0.1169E-04 |
| 20 (BSC. Malindi) | 0.1003E-04 | 0.1125 E-04 | 0.1034E-04 | 0.1167E-04 |
| 21 (BSC. Malindi) | 0.0991E-04 | 0.1110 E-04 | 0.1036E-04 | 0.1171E-04 |
| Tropical | 0.1005E-04 | 0.1123 E-04 | 0.1050E-04 | 0.1187E-04 |
| Midlatitude summer | 0.0946E-04 | 0.1065 E-04 | 0.0977E-04 | 0.1107E-04 |
| Mid latitude winter | 0.0650 E-04 | 0.0758 E-04 | 0.0662E-04 | 0.0773E-04 |
| Subarctic summer | 0.0824E-04 | 0.0934 E-04 | 0.0850E-04 | 0.0970E-04 |
| Subarctic winter | 0.0539E-04 | 0.0610 E-04 | 0.0544E-04 | 0.0615E-04 |
| US standard | 0.0801E-04 | 0.0925 E-04 | 0.0830E-04 | 0.0962E-04 |

Table 5.5 shows the ratio of downwelling to upwelling atmospheric mean radiance, $z_i$ and absorptance $(1-\tau_i)$, while Figures 5.1 a and 5.1 b shows the variation of $z_i$ with atmospheric absorptance $(1-\tau_i)$ for $(i = 31, 32)$. It is evident that the ratio $z_i$ is slightly greater than one, implying that downwelling atmospheric mean radiance is slightly greater than upwelling atmospheric mean radiance. This is because the lower layers of the atmosphere, which contribute more to the reflected downwelling radiance, are warmer.

Once the spectral radiances were simulated, the corresponding brightness temperatures for MODIS bands 31 $(T_{31})$ and 32 $(T_{32})$ and the beta term $(\beta)$ were evaluated, their results are shown in Table 5.6.

### 5.2.3 Coefficients $a_i$ and $a_i^{'}$

The coefficients $a_i$ and $a_i^{'}$ $(i = 1, 2, 3)$, for assumed emissivities of 0.9 and 1 respectively, were computed for a range of atmospheric water vapor between 0.4 g cm$^{-2}$ to 5.4 g cm$^{-2}$. The results of evaluation of these coefficients are shown in Table 5.7 while Figure 5.2 shows their variation with atmospheric water vapour. It can be seen that $a_2$ is more sensitive to the surface emittance effect than $a_1$ and $a_3$, while $a_2$ and to a lesser degree $a_3$ are significantly influenced by atmospheric water vapour absorption. Regressive relationships for the two values of mean surface emittance are respectively:

$$\begin{cases} a_2^{'}(\overline{\varepsilon}=1) = 0.34w + 1.5 \\ a_3^{'}(\overline{\varepsilon}=1) = 0.02w - 0.01 \end{cases} \begin{cases} a_2(\overline{\varepsilon}=0.9) = 0.39w + 1.7 \\ a_3(\overline{\varepsilon}=0.9) = 0.023w - 0.015 \end{cases} \tag{5.2}$$

**Table 5.5: Results of evaluation of $z_{31}$, $z_{32}$, $(1-\tau_{31})$ and $(1-\tau_{32})$**

| Profile | $z_{31}$ | $z_{32}$ | $(1-\tau_{31})$ | $(1-\tau_{32})$ |
|---|---|---|---|---|
| 01 (BSC. Malindi) | 1.0598 | 1.0773 | 0.5707 | 0.7068 |
| 02 (BSC. Malindi) | 1.0486 | 1.0628 | 0.4320 | 0.5584 |
| 03 (BSC. Malindi) | 1.0264 | 1.0329 | 0.3233 | 0.4320 |
| 04 (BSC. Malindi) | 1.0445 | 1.0555 | 0.4695 | 0.6014 |
| 05 (BSC. Malindi) | 1.0492 | 1.0613 | 0.4727 | 0.6045 |
| 06 (BSC. Malindi) | 1.0361 | 1.0458 | 0.4733 | 0.6060 |
| 07 (BSC. Malindi) | 1.0367 | 1.0453 | 0.3094 | 0.4150 |
| 08 (BSC. Malindi) | 1.0507 | 1.0631 | 0.4404 | 0.5699 |
| 09 (BSC. Malindi) | 1.0348 | 1.0423 | 0.3040 | 0.4074 |
| 10 (BSC. Malindi) | 1.0636 | 1.0806 | 0.4802 | 0.6128 |
| 11 (BSC. Malindi) | 1.0405 | 1.0513 | 0.4062 | 0.5298 |
| 12 (BSC. Malindi) | 1.0423 | 1.0513 | 0.3625 | 0.4771 |
| 13 (BSC. Malindi) | 1.0480 | 1.0607 | 0.4932 | 0.6267 |
| 14 (BSC. Malindi) | 1.0560 | 1.0717 | 0.5120 | 0.6475 |
| 15 (BSC. Malindi) | 1.0577 | 1.0731 | 0.4888 | 0.6236 |
| 16 (BSC. Malindi) | 1.0380 | 1.0466 | 0.2887 | 0.3890 |
| 17 (BSC. Malindi) | 1.0490 | 1.0630 | 0.4813 | 0.6151 |
| 18 (BSC. Malindi) | 1.0411 | 1.0504 | 0.3183 | 0.4231 |
| 19 (BSC. Malindi) | 1.0413 | 1.0498 | 0.4023 | 0.5256 |
| 20 (BSC. Malindi) | 1.0308 | 1.0374 | 0.4032 | 0.5269 |
| 21 (BSC. Malindi) | 1.0453 | 1.0553 | 0.4067 | 0.5292 |
| Tropical | 1.0449 | 1.0565 | 0.4360 | 0.5633 |
| Midlatitude summer | 1.0327 | 1.0401 | 0.2856 | 0.3857 |
| Midlatitude winter | 1.0194 | 1.0191 | 0.0569 | 0.0836 |
| Subarctic summer | 1.0323 | 1.0380 | 0.1810 | 0.2544 |
| Subarctic winter | 1.0108 | 1.0090 | 0.0213 | 0.0334 |
| US standard | 1.0357 | 1.0397 | 0.1070 | 0.1511 |

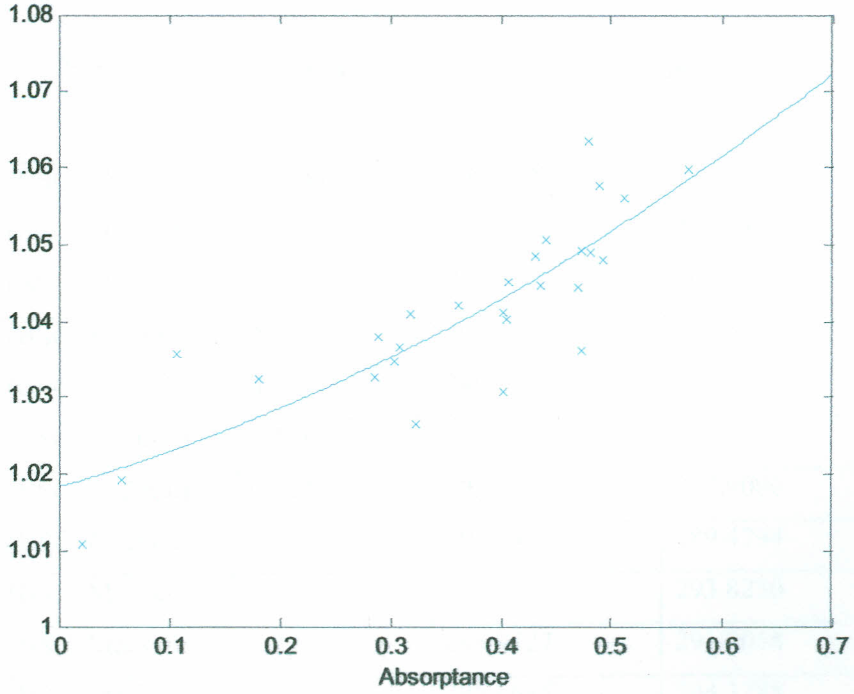

**Figure 5.1 a: The ratio $z_{31}$ *versus* atmospheric absorptance, $(1-\tau_{31})$**

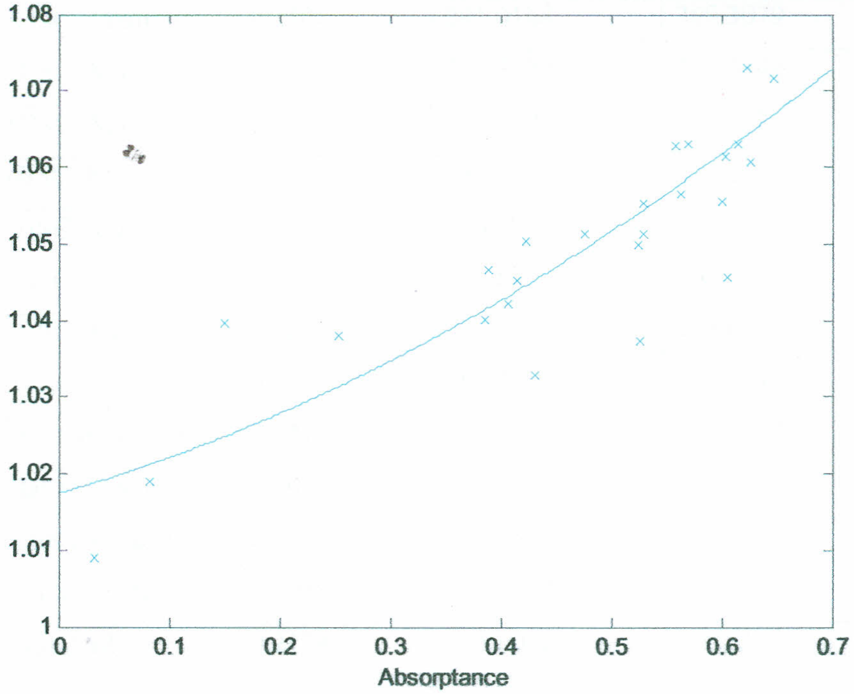

**Figure 5.1 b: The ratio $z_{32}$ *versus* atmospheric absorptance, $(1-\tau_{32})$**

**Table 5.6: Results of evaluation of the beta term and brightness temperature**

| Profile | Beta | Brightness temperature (K) | |
|---|---|---|---|
| | | $T_{31}$ | $T_{32}$ |
| 01 (BSC. Malindi) | 0.2243 | 296.2498 | 294.4297 |
| 02 (BSC. Malindi) | 0.2241 | 295.9937 | 294.5111 |
| 03 (BSC. Malindi) | 0.2223 | 293.3762 | 292.6580 |
| 04 (BSC. Malindi) | 0.2233 | 294.7565 | 293.3021 |
| 05 (BSC. Malindi) | 0.2247 | 296.7610 | 295.2375 |
| 06 (BSC. Malindi) | 0.2215 | 292.2776 | 291.2057 |
| 07 (BSC. Malindi) | 0.2226 | 293.8909 | 292.9096 |
| 08 (BSC. Malindi) | 0.2206 | 291.0478 | 289.4794 |
| 09 (BSC. Malindi) | 0.2232 | 294.7457 | 293.8230 |
| 10 (BSC. Malindi) | 0.2227 | 293.9727 | 291.8058 |
| 11 (BSC. Malindi) | 0.2239 | 295.6635 | 294.3788 |
| 12 (BSC. Malindi) | 0.2253 | 297.6400 | 296.5917 |
| 13 (BSC. Malindi) | 0.2244 | 296.4104 | 294.9949 |
| 14 (BSC. Malindi) | 0.2228 | 294.1829 | 292.3995 |
| 15 (BSC. Malindi) | 0.2206 | 291.0168 | 289.3079 |
| 16 (BSC. Malindi) | 0.2222 | 293.3077 | 292.4440 |
| 17 (BSC. Malindi) | 0.2206 | 291.0927 | 289.5521 |
| 18 (BSC. Malindi) | 0.2254 | 297.6974 | 296.6325 |
| 19 (BSC. Malindi) | 0.2234 | 294.9908 | 293.7629 |
| 20 (BSC. Malindi) | 0.2232 | 294.6784 | 293.6818 |
| 21 (BSC. Malindi) | 0.2234 | 294.9075 | 293.6727 |
| Tropical | 0.2238 | 295.4603 | 294.1176 |
| Midlatitude summer | 0.2211 | 291.7009 | 291.0239 |
| Midlatitude winter | 0.2064 | 271.4660 | 271.4534 |
| Subarctic summer | 0.2164 | 285.2340 | 284.6690 |
| Subarctic winter | 0.1958 | 257.0050 | 257.2326 |
| US standard | 0.2174 | 286.6072 | 286.2890 |

**Table 5.7: Results of evaluation of coefficients $a_i$ and $a_i^{'}$**

| profile | $a_1^{'}$ | $a_2^{'}$ | $a_3^{'}$ | $a_1$ | $a_2$ | $a_3$ |
|---|---|---|---|---|---|---|
| 01 (BSC. Malindi) | 1.0000 | 3.4717 | 0.0982 | 1.0568 | 3.9011 | 0.1138 |
| 02 (BSC. Malindi) | 1.0000 | 2.9037 | 0.0649 | 1.0765 | 3.2783 | 0.0767 |
| 03 (BSC. Malindi) | 1.0000 | 2.5660 | 0.0443 | 1.0891 | 2.8991 | 0.0530 |
| 04 (BSC. Malindi) | 1.0000 | 3.0101 | 0.0724 | 1.0714 | 3.3970 | 0.0852 |
| 05 (BSC. Malindi) | 1.0000 | 3.0288 | 0.0732 | 1.0709 | 3.4177 | 0.0861 |
| 06 (BSC. Malindi) | 1.0000 | 3.0157 | 0.0731 | 1.0710 | 3.4030 | 0.0859 |
| 07 (BSC. Malindi) | 1.0000 | 2.5324 | 0.0420 | 1.0906 | 2.8603 | 0.0504 |
| 08 (BSC. Malindi) | 1.0000 | 2.8925 | 0.0659 | 1.0751 | 3.2668 | 0.0779 |
| 09 (BSC. Malindi) | 1.0000 | 2.5416 | 0.0414 | 1.0911 | 2.8703 | 0.0497 |
| 10 (BSC. Malindi) | 1.0000 | 3.0556 | 0.0749 | 1.0698 | 3.4470 | 0.0880 |
| 11 (BSC. Malindi) | 1.0000 | 2.8043 | 0.0594 | 1.0797 | 3.1679 | 0.0705 |
| 12(BSC. Malindi) | 1.0000 | 2.7093 | 0.0517 | 1.0847 | 3.0610 | 0.0616 |
| 13 (BSC. Malindi) | 1.0000 | 3.1107 | 0.0780 | 1.0681 | 3.5077 | 0.0914 |
| 14 (BSC. Malindi) | 1.0000 | 3.1735 | 0.0822 | 1.0654 | 3.5764 | 0.0961 |
| 15 (BSC. Malindi) | 1.0000 | 3.0599 | 0.0763 | 1.0686 | 3.4517 | 0.0896 |
| 16 (BSC. Malindi) | 1.0000 | 2.4926 | 0.0388 | 1.0927 | 2.8139 | 0.0466 |
| 17 (BSC. Malindi) | 1.0000 | 3.0378 | 0.0747 | 1.0698 | 3.4271 | 0.0878 |
| 18 (BSC. Malindi) | 1.0000 | 2.6134 | 0.0442 | 1.0896 | 2.9510 | 0.0530 |
| 19 (BSC. Malindi) | 1.0000 | 2.7875 | 0.0586 | 1.0799 | 3.1500 | 0.0695 |
| 20 (BSC. Malindi) | 1.0000 | 2.7840 | 0.0587 | 1.0799 | 3.1460 | 0.0696 |
| 21 (BSC. Malindi) | 1.0000 | 2.8307 | 0.0599 | 1.0794 | 3.1978 | 0.0711 |
| Tropical | 1.0000 | 2.9085 | 0.0655 | 1.0758 | 3.2843 | 0.0774 |
| Midlatitude summer | 1.0000 | 2.4724 | 0.0381 | 1.0930 | 2.7914 | 0.0458 |
| Midlatitude winter | 1.0000 | 1.8919 | 0.0063 | 1.1091 | 2.1137 | 0.0077 |
| subarctic summer | 1.0000 | 2.1652 | 0.0220 | 1.1020 | 2.4368 | 0.0267 |
| Subarctic winter | 1.0000 | 1.5844 | 0.0021 | 1.1105 | 1.7653 | 0.0026 |
| US standard | 1.0000 | 2.1352 | -0.0155 | 0.8109 | 2.3919 | -0.0188 |

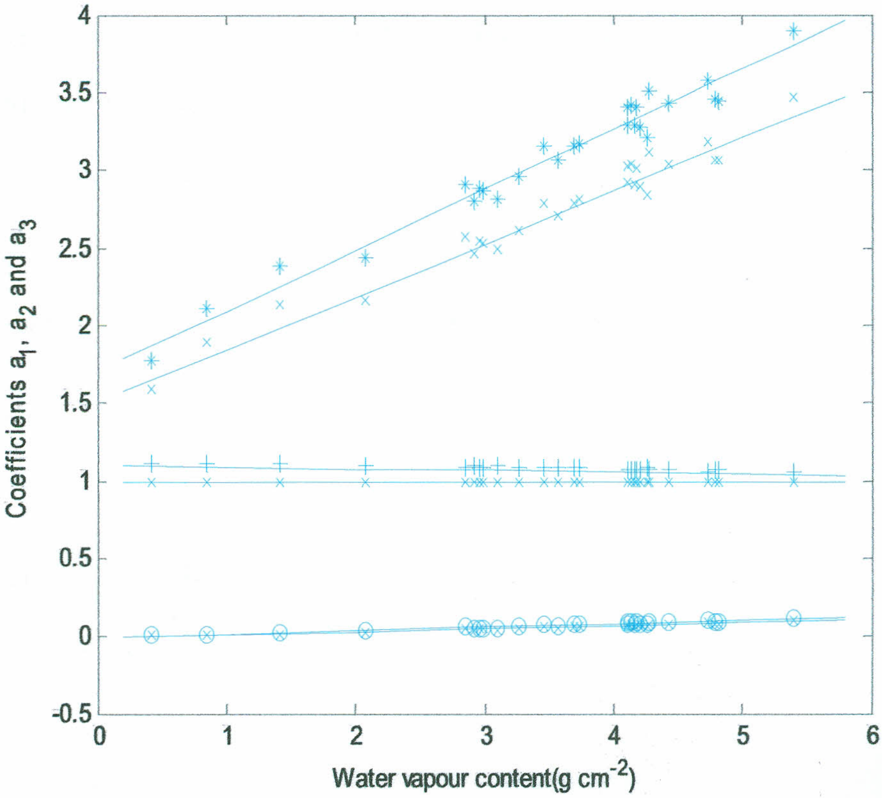

**Figure 5.2: Coefficients $a_i$ and $a_i'$ *versus* total water vapour content for two values of mean surface emittance: $\bar{\varepsilon} = 0.9$ (+) $a_1$, (*) $a_2$, (o) $a_3$, $\bar{\varepsilon} = 1$ (×) $a'_{1,2,3}$**

### 5.3 The proposed sensible heat flux algorithm

Using the modified General Split Widow Technique (GSWT) algorithm, equation (4.25), and the bulk aerodynamic resistance, equation (2.2), sensible heat flux $(H)$ can be formulated as:

$$H = \rho C_p r^{-1}\left\{T_{31} + a_2'(T_{31} - T_{32}) + F_1(1-\bar{\varepsilon}) + F_2\delta\varepsilon + F_3\left((1-\bar{\varepsilon})^2 - (0.5\delta\varepsilon)^2\right) + F_4(T_s - T_a) - T_a\right\}$$

Or

$$\begin{aligned} H = {} & \rho C_p r^{-1}\left\{T_{31} + a_2'(T_{31} - T_{32}) + F_1(1-\bar{\varepsilon}) + F_2\delta\varepsilon + F_3\left((1-\bar{\varepsilon})^2 - (0.5\delta\varepsilon)^2\right) - T_a\right\} \\ & + \rho C_p r^{-1} F_4 (T_s - T_a) \end{aligned} \qquad (5.3)$$

It follows that:

$$H = \rho C_p r^{-1} h + \rho C_p r^{-1} F_4 (T_s - T_a) \qquad (5.4)$$

where

$$h = T_{31} + a_2'(T_{31} - T_{32}) + F_1(1-\bar{\varepsilon}) + F_2\delta\varepsilon + F_3\left((1-\bar{\varepsilon})^2 - (0.5\delta\varepsilon)^2\right) - T_a \qquad (5.5)$$

and all other terms have previously been defined elsewhere in this work

Again, substituting for $T_s$ from equation (4.25) into equation (5.4), we have:

$$H = \rho C_p r^{-1} h$$
$$+ \rho C_p r^{-1} F_4 \left[T_{31} + a_2'(T_{31} - T_{32}) + F_1(1-\bar{\varepsilon}) + F_2\delta\varepsilon + F_3\left((1-\bar{\varepsilon})^2 - (0.5\delta\varepsilon)^2\right) + F_4(T_s - T_a) - T_a\right]$$

Or

$$H = \rho C_p r^{-1} h$$
$$+\rho C_p r^{-1} F_4 \left[T_{31} + a_2'(T_{31} - T_{32}) + F_1(1-\bar{\varepsilon}) + F_2\delta\varepsilon + F_3\left((1-\bar{\varepsilon})^2 - (0.5\delta\varepsilon)^2\right) - T_a\right]$$
$$+ \rho C_p r^{-1} (F_4)^2 (T_s - T_a)$$

and therefore

$$H = \rho C_p r^{-1} h + \rho C_p r^{-1} h F_4 + \rho C_p r^{-1} (F_4)^2 (T_s - T_a) \qquad (5.6)$$

Similarly, substituting for $T_s$ from equation (4.25) into equation (5.6), we have:

$$H = \rho C_p r^{-1} h$$
$$+\rho C_p r^{-1} h F_4$$
$$+ \rho C_p r^{-1} (F_4)^2 \left[T_{31} + a_2'(T_{31} - T_{32}) + F_1(1-\bar{\varepsilon}) + F_2\delta\varepsilon + F_3\left((1-\bar{\varepsilon})^2 - (0.5\delta\varepsilon)^2\right) + F_4(T_s - T_a) - T_a\right]$$

Or

$$H = \rho C_p r^{-1} h + \rho C_p r^{-1} h F_4$$
$$+\rho C_p r^{-1} (F_4)^2 \left[T_{31} + a_2'(T_{31} - T_{32}) + F_1(1-\bar{\varepsilon}) + F_2\delta\varepsilon + F_3\left((1-\bar{\varepsilon})^2 - (0.5\delta\varepsilon)^2\right) - T_a\right] +$$
$$+\rho C_p r^{-1} (F_4)^3 (T_s - T_a)$$

resulting in

$$H = \rho C_p r^{-1} h + \rho C_p r^{-1} h F_4 + \rho C_p r^{-1} (F_4)^2 h + \rho C_p r^{-1} (F_4)^3 (T_s - T_a) \quad (5.7)$$

This process can be continued up to the desired term. Continuing this process $n$ times we eventually get:

$$H_n = \rho C_p r^{-1} h + \rho C_p r^{-1} h F_4 + \rho C_p r^{-1} h (F_4)^2 + \rho C_p r^{-1} h (F_4)^3 + \dots\dots\dots + \rho C_p r^{-1} h (F_4)^{n-1} + \rho C_p r^{-1} (F_4)^n (T_s - T_a) \quad (5.8)$$

Multiplying equation (5.8) by $F_4$ we have:

$$F_4 H_n = \rho C_p r^{-1} h F_4 + \rho C_p r^{-1} h (F_4)^2 + \rho C_p r^{-1} h (F_4)^3 + \rho C_p r^{-1} h (F_4)^4 + \dots\dots\dots + \rho C_p r^{-1} h (F_4)^n + \rho C_p r^{-1} (F_4)^{n+1} (T_s - T_a) \quad (5.9)$$

Subtracting equation (5.9) from equation (5.8), the following equation results:

$$H_n - F_4 H_n = \rho C_p r^{-1} h - \rho C_p r^{-1} h (F_4)^n - \rho C_p r^{-1} (F_4)^{n+1} (T_s - T_a) + \rho C_p r^{-1} (F_4)^n (T_s - T_a) \quad (5.10)$$

Or

$$H_n (1 - F_4) = \rho C_p r^{-1} h (1 - (F_4)^n) + \rho C_p r^{-1} (F_4)^n (T_s - T_a)(1 - F_4) \quad (5.11)$$

and we finally have:

$$H_n = \frac{\rho C_p r^{-1} h(1-(F_4{}^n))}{(1-F_4)} + \rho C_p r^{-1} (F_4)^n (T_s - T_a) \tag{5.12}$$

Equation (5.12) is our new formulation of sensible heat flux resulting from the modified GSWT algorithm for surface temperature retrieval. However, for completeness, the aerodynamic resistance $(r)$ appearing in this equation need to be known. It depends on several parameters, including aerodynamic properties of the canopy surface and atmospheric stability, and therefore its accurate retrieval posses a significant challenge in the sensible heat flux determination. Section 5.3.1 explains how this factor is estimated using the modified GSWT algorithm, equation (4.25).

### 5.3.1 Parametization of aerodynamic resistance

Here, the model developed by Choudhury–2 *et al.*, 1986 (equation 3.52) based on different atmospheric stabilities was used to perform stability corrections for retrieval of sensible heat flux. The model gives results which are in good agreement with measured values (Liu *et al.*, 2007). It is convenient to use since no iteration is required (Watts *et al.*, 2000). Since the stability factor $(\eta)$ in equation (3.53) depends on the difference between surface and air temperatures it can be expressed, using the modified GSWT algorithm equation (4.25), as:

$$\eta = \frac{5(z-d)g}{T_a u^2}\left[T_{31} + a_2'(T_{31} - T_{32}) + F_1(1-\overline{\varepsilon}) + F_2 \delta\varepsilon + F_3\left((1-\overline{\varepsilon})^2 - (0.5\delta\varepsilon)^2\right) + F_4(T_s - T_a) - T_a\right]$$

Or

$$\eta = \frac{5(z-d)g}{T_a u^2}\left[T_{31} + a_2'(T_{31} - T_{32}) + F_1(1-\bar{\varepsilon}) + F_2\delta\varepsilon + F_3\left((1-\bar{\varepsilon})^2 - (0.5\delta\varepsilon)^2\right) - T_a\right]$$
$$+ \rho C_p r^{-1} F_4 (T_s - T_a)$$

Resulting in:

$$\eta = \frac{5(z-d)g}{T_a u^2} h + \frac{5(z-d)g}{T_a u^2} F_4 (T_s - T_a) \tag{5.13}$$

Substituting for $(T_s)$ from equation (4.25) into equation (5.13), we have:

$$\begin{aligned}\eta = {} & \frac{5(z-d)g}{T_a u^2} h \\ & + \frac{5(z-d)g}{T_a u^2} F_4\left[T_{31} + a_2'(T_{31} - T_{32}) + F_1(1-\bar{\varepsilon}) + F_2\delta\varepsilon + F_3\left((1-\bar{\varepsilon})^2 - (0.5\delta\varepsilon)^2\right) - T_a\right] \\ & + \frac{5(z-d)g}{T_a u^2} (F_4)^2 (T_s - T_a)\end{aligned} \tag{5.14}$$

and finally:

$$\eta = \frac{5(z-d)g}{T_a u^2} h + \frac{5(z-d)g}{T_a u^2} h F_4 + \frac{5(z-d)g}{T_a u^2} (F_4)^2 (T_s - T_a) \tag{5.15}$$

Therefore, continuing this process $n$ times we finally get:

$$\begin{aligned}\eta_n = {} & \frac{5(z-d)g}{T_a u^2} h + \frac{5(z-d)g}{T_a u^2} h F_4 + \frac{5(z-d)g}{T_a u^2} (F_4)^2 + \frac{5(z-d)g}{T_a u^2} h (F_4)^3 \\ & + \dots\dots\dots + \frac{5(z-d)g}{T_a u^2} h (F_4)^{n-1} + \frac{5(z-d)g}{T_a u^2} (F_4)^n (T_s - T_a)\end{aligned} \tag{5.16}$$

Multiplying equation (5.16) by $F_4$ we have:

$$F_4\eta_n = \frac{5(z-d)g}{T_a u^2} hF_4 + \frac{5(z-d)g}{T_a u2} h(F_4)^2 + \frac{5(z-d)g}{T_a u^2} h(F_4)^3 + \frac{5(z-d)g}{T_a u^2} h(F_4)^4$$
$$+ \ldots\ldots\ldots + \frac{5(z-d)g}{T_a u^2} h(F_4)^n + \frac{5(z-d)g}{T_a u2} (F_4)^{n+1}(T_s - T_a) \qquad (5.17)$$

Subtracting equation (5.17) from (5.16) and re–arranging, the stability factor for aerodynamic resistance is given by:

$$\eta_n = \frac{5(z-d)gh(1-(F_4)^n)}{T_a u^2(1-F_4)} + \frac{5(z-d)g}{T_a u^2}(F_4)^n (T_s - T_a) \qquad (5.18)$$

Therefore, from equations (3.60), (3.62) and (5.18), we have:

$$r_n = \frac{r_o}{\left\{1 + \frac{5(z-d)g}{T_a u^2}\left(\frac{h(1-(F_4)^n)}{(1-F_4)} + (F_4)^n (T_s - T_a)\right)\right\}^p} \qquad (5.19)$$

as our expression for the aerodynamic resistance in our new formulation.

### 5.3.2 Assessment of effects

Substituting for $r_n$ from equation 5.19 into equation (5.12) it follows that:

$$H_n = \frac{\rho C_p \frac{\left\{1+\left(\frac{5(z-d)gh(1-(F_4)^n)}{T_a u^2(1-F_4)}+\frac{5(z-d)g}{T_a u^2}(F_4)^n(T_s-T_a)\right)\right\}^p}{r_o} h(1-(F_4)^n)}{(1-F_4)} + \rho C_p \frac{\left\{1+\left(\frac{5(z-d)gh(1-(F_4)^n)}{T_a u^2(1-F_4)}+\frac{5(z-d)g}{T_a u^2}(F_4)^n(T_s-T_a)\right)\right\}^p}{r_o}(F_4)^n(T_s-T_a) \qquad (5.2)$$

Or

$$H_n = \frac{\rho C_p h(1-(F_4)^n)\left\{1+\left(\frac{5(z-d)gh(1-(F_4)^n)}{T_a u^2(1-F_4)}+\frac{5(z-d)g}{T_a u^2}(F_4)^n(T_s-T_a)\right)\right\}^p}{r_o(1-F_4)} + \frac{\rho C_p (F_4)^n(T_s-T_a)\left\{1+\left(\frac{5(z-d)gh(1-(F_4)^n)}{T_a u^2(1-F_4)}+\frac{5(z-d)g}{T_a u^2}(F_4)^n(T_s-T_a)\right)\right\}^p}{r_o} \qquad (5.21)$$

Rearranging equation (5.21), we eventually have:

$$H = H_{n(n\to\infty)} =$$

$$\frac{\rho C_p}{r_o}\left\{\frac{h(1-(F_4)^n)}{(1-F_4)}+(F_4)^n(T_s-T_a)\right\}\left\{1+\frac{5(z-d)g}{T_a u^2}\left(\frac{h(1-(F_4)^n)}{(1-F_4)}+(F_4)^n(T_s-T_a)\right)\right\}^p \qquad (5.22)$$

Equation (5.22) is the proposed general algorithm for determination of sensible heat flux. This equation is assessed based on different atmospheric stabilities and taking into account that $F_4$ is always less than one, as evidenced from simulation results in Table 5.8 and Figure 5.3.

**Table 5.8: Values of $F_4$ for the atmospheric situations considered**

| Profile | $F_4$<br>($\varepsilon_{31}$=0.99, $\varepsilon_{32}$=0.97) | $F_4$<br>($\varepsilon_{31}$=0.95, $\varepsilon_{32}$=0.93) | $F_4$<br>($\varepsilon_{31}$=0.89, $\varepsilon_{32}$=0.91) |
|---|---|---|---|
| 01(BSC.Malindi) | 0.0970 | 0.1028 | 0.1190 |
| 02 (BSC.Malindi) | 0.0635 | 0.0678 | 0.0813 |
| 03 (BSC.Malindi) | 0.0431 | 0.0463 | 0.0569 |
| 04 (BSC.Malindi) | 0.0712 | 0.0758 | 0.0899 |
| 05 (BSC.Malindi) | 0.0720 | 0.0767 | 0.0909 |
| 06 (BSC.Malindi) | 0.0719 | 0.0765 | 0.0907 |
| 07 (BSC.Malindi) | 0.0409 | 0.0439 | 0.0541 |
| 08 (BSC.Malindi) | 0.0647 | 0.0690 | 0.0825 |
| 09 (BSC.Malindi) | 0.0402 | 0.0432 | 0.0534 |
| 10 (BSC.Malindi) | 0.0736 | 0.0784 | 0.0929 |
| 11 (BSC.Malindi) | 0.0582 | 0.0622 | 0.0749 |
| 12 (BSC.Malindi) | 0.0504 | 0.0540 | 0.0659 |
| 13 (BSC.Malindi) | 0.0767 | 0.0816 | 0.0963 |
| 14 (BSC.Malindi) | 0.0810 | 0.0861 | 0.1011 |
| 15 (BSC.Malindi) | 0.0751 | 0.0800 | 0.0944 |
| 16 (BSC.Malindi) | 0.0376 | 0.0404 | 0.0502 |
| 17 (BSC.Malindi) | 0.0735 | 0.0783 | 0.0926 |
| 18 (BSC.Malindi) | 0.0430 | 0.0461 | 0.0569 |
| 19 (BSC.Malindi) | 0.0573 | 0.0613 | 0.0740 |
| 20 (BSC.Malindi) | 0.0574 | 0.0614 | 0.0740 |
| 21 (BSC.Malindi) | 0.0586 | 0.0627 | 0.0756 |
| Tropical | 0.0642 | 0.0686 | 0.0821 |
| Midlatitude summer | 0.0370 | 0.0398 | 0.0493 |
| Midlatitude winter | 0.0061 | 0.0066 | 0.0085 |
| Subarctic summer | 0.0213 | 0.0229 | 0.0290 |
| Subarctic winter | 0.0020 | 0.0022 | 0.0028 |
| US standard | 0.0123 | 0.0133 | 0.0173 |

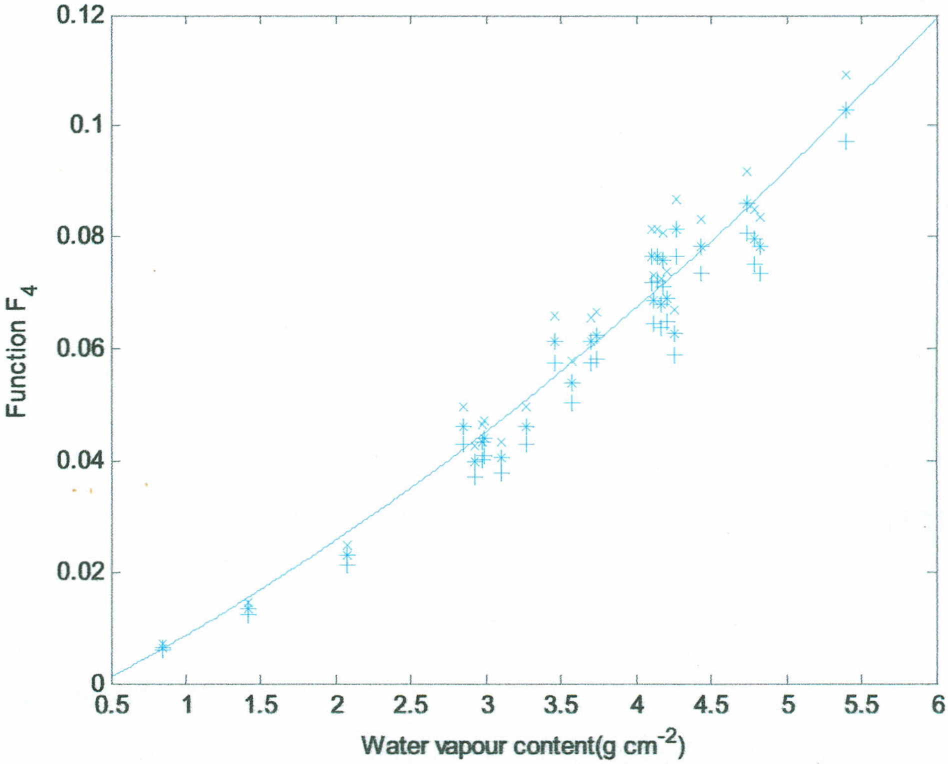

**Figure 5.3: The function** $F_4$ **:** $\bar{\varepsilon} = 0.98\,(+)$**,** $\bar{\varepsilon} = 0.94\,(*)$**,** $\bar{\varepsilon} = 0.90\,(\times)$ ***versus* water vapour column (WVC)**

It is evident how they are highly sensitive to water vapour but is scarcely influenced by the surface emittance effect. It varies with water vapor column $(w)$ according to:

$$F_4 = 0.0013w^2 + 0.013w - 0.0057 \qquad (5.23)$$

### 5.3.2.1 Neutral conditions

Under neutral conditions, aerodynamic resistance is evaluated for $p = 0$. Since $F_4$ is always less than one, then $(F_4)^n \approx 0$. Therefore, the sensible heat flux equation (5.22) reduces to:

$$H_{neutral} = \frac{\rho\, C_P}{r_o}\frac{h}{(1-F_4)} \tag{5.24}$$

### 5.3.2.2 Stable conditions

For stable atmospheric conditions, air temperature is always greater than surface temperature $(T_a > T_s)$. Aerodynamic resistance is evaluated for $p = 2$. Therefore the sensible heat flux equation (5.22) becomes:

$$H_{stable} = \frac{\rho\, C_P}{r_o}\frac{h}{(1-F_4)}\left(1+\frac{5(z-d)g}{T_a u^2}\frac{h}{(1-F_4)}\right)^2 \tag{5.25}$$

### 5.3.2.3 Unstable conditions

Finally, for unstable environmental condition surface temperature is always greater than air temperature $(T_s > T_a)$. Aerodynamic resistance is evaluated for $p = 0.75$ and sensible heat flux can be evaluated from equation (5.22) as:

$$H_{unstable} = \frac{\rho\, C_P}{r_o}\frac{h}{(1-F_4)}\left(1+\frac{5(z-d)g}{T_a u^2}\frac{h}{(1-F_4)}\right)^{0.75} \tag{5.26}$$

Combining equations (5.24), (5.25) and (5.26) the following simple general algorithm for determination of sensible heat flux results:

$$H = \frac{\rho\, C_P}{r_o}k\left(1+\frac{5(z-d)g}{T_a u^2}k\right)^p \tag{5.27}$$

where all the symbols have previously been defined elsewhere in this work and

$$k = 1.06\left(T_{31} + a_2'(T_{31} - T_{32}) - T_a\right) + k_1(1-\bar{\varepsilon}) + k_2\delta\varepsilon + k_3\left((1-\bar{\varepsilon})^2 - (0.5\delta\varepsilon)^2\right) \qquad (5.28)$$

Equation 5.28 was solved by linear regression analysis with least–square–sum fitting using 21 sets of emissivity conditions shown in Table 5.6. Table 5.7 shows the values of $k_1$, $k_2$ and $k_3$ evaluated while their variations with atmospheric water vapour content are illustrated in Figure 5.4. It is evident how they are scarcely influenced if the atmospheric water vapour content is $\leq 3.0$ g cm$^{-2}$. The mean values of these coefficients within this water vapour range are: $k_1 = 61.92$, $k_2 = -125.47$, $k_3 = 48.63$ and $a_2' = 2.24$.

For any realistic amount of atmospheric water vapour content above 3.0 g cm$^{-2}$, the following regressive relationships fit very well the behavior of $k_1$, $k_2$ and $k_3$ *versus* atmospheric water vapour content $(w)$:

$$\begin{cases} k_1 = -7.2w + 84 \\ k_2 = 23w - 180 \\ k_3 = -4.4w + 66 \end{cases} \qquad (5.29)$$

**Table 5.10: Values of $k_1$, $k_2$ and $k_3$ for the atmospheric situations considered**

| Profile | $k_1$ | $k_2$ | $k_3$ |
|---|---|---|---|
| 01 (BSC. Malindi) | 44.704014 | -58.731555 | 40.396941 |
| 02 (BSC. Malindi) | 55.431972 | -87.650139 | 48.9132135 |
| 03 (BSC. Malindi) | 59.888145 | -106.6587915 | 51.1759125 |
| 04 (BSC. Malindi) | 51.678273 | -77.317935 | 46.5169635 |
| 05 (BSC. Malindi) | 52.3480515 | -78.022326 | 46.380963 |
| 06 (BSC. Malindi) | 49.1730735 | -72.0015615 | 44.7980535 |
| 07 (BSC. Malindi) | 61.889493 | -113.0142855 | 52.301937 |
| 08 (BSC. Malindi) | 53.1734265 | -82.689795 | 48.0752715 |
| 09 (BSC. Malindi) | 62.372364 | -115.5308805 | 52.6588185 |
| 10 (BSC. Malindi) | 53.326041 | -80.3897145 | 47.1110205 |
| 11 (BSC. Malindi) | 56.5948455 | -91.8672195 | 49.6278285 |
| 12 (BSC. Malindi) | 59.855343 | -103.195305 | 50.863548 |
| 13 (BSC. Malindi) | 49.9671375 | -72.1894275 | 45.5861535 |
| 14 (BSC. Malindi) | 49.0437825 | -69.7141545 | 45.287634 |
| 15 (BSC. Malindi) | 49.813032 | -72.334587 | 45.245673 |
| 16 (BSC. Malindi) | 62.676741 | -117.441171 | 52.191177 |
| 17 (BSC. Malindi) | 49.9488195 | -73.159962 | 45.004557 |
| 18 (BSC. Malindi) | 63.2807025 | -116.6787375 | 52.157949 |
| 19 (BSC. Malindi) | 56.270766 | -91.6929855 | 49.83987 |
| 20 (BSC. Malindi) | 55.3430445 | -89.400786 | 48.9304665 |
| 21 (BSC. Malindi) | 56.028159 | -91.4787075 | 49.370844 |
| Tropical | 54.367398 | -85.0152225 | 47.955033 |
| Midlatitude summer | 61.627716 | -114.804231 | 51.427359 |
| Midlatitude winter | 61.8033345 | -143.162625 | 42.880734 |
| subarctic summer | 64.4490075 | -132.6239175 | 50.064372 |
| Subarctic winter | 55.2806355 | -119.626551 | 42.2754945 |
| US standard | 68.0599965 | -158.3696535 | 46.285965 |

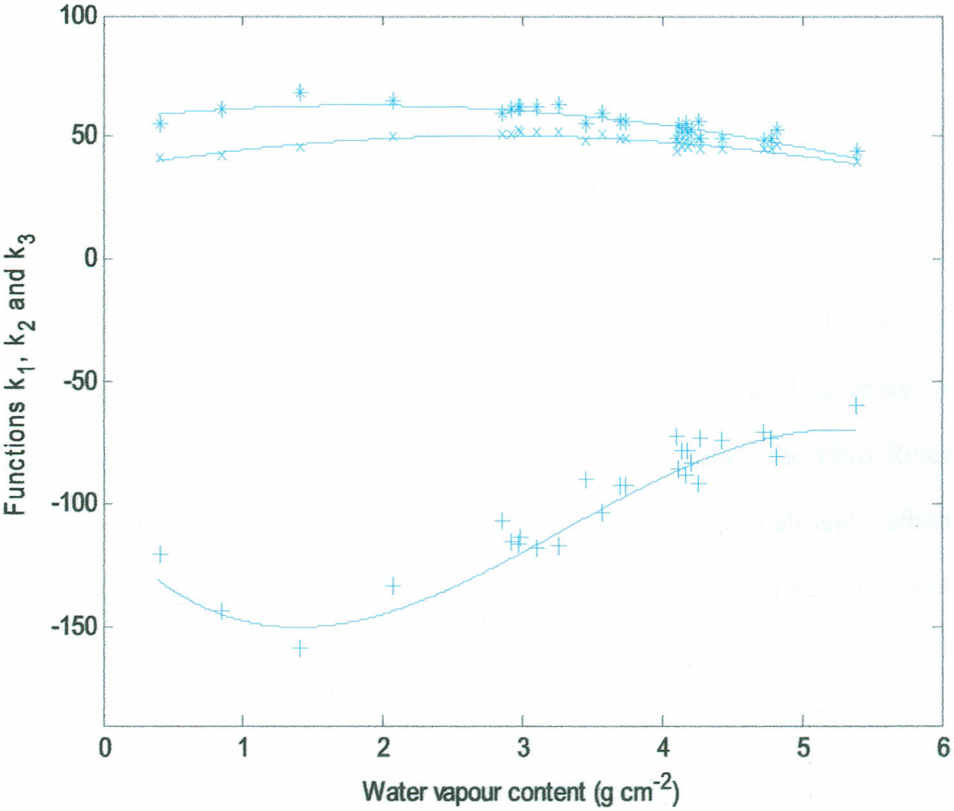

**Figure 5.4: The $k_1$ (*), $k_2$ (+) and $k_3$ (×) functions *versus* water vapour content.**

## 5.4 Validation of the algorithm

The quantitative validation of the proposed algorithm was done using MODIS data in coincidence with *in situ* measurements of sensible heat flux. In the MODIS sensible heat flux processing, MODIS Calibrated Radiance (MOD021KM), emissivity product (MOD11_L2) and water vapour product (MOD 05_L2) from ftp://ladsweb.nascom.nasa.gov were used to retrieve $H$ pixel by pixel. The *in situ* data were obtained from a series of field campaigns conducted by University of Lleida, Spain between 15th April, 2004 to 26th July, 2004 within the Ebro River basin, Spain (41°18'04''N, 0°21'51"W, elevation 150 m). The materials and method used in determination of the *in situ* sensible heat flux are described in detail elsewhere (Castellvi and Martínez-Cob, 2005).

These data were extracted to coincide as closely as possible with satellite overpass (nearest 30 minutes average). A summary of data used in validation process as well as validation results for neutral, stable and unstable atmospheric conditions are given in Tables 5.11, 5.12 and 5.13 respectively. Figures 5.5, 5.6 and 5.7 shows specific comparison between measured sensible heat flux and MODIS based sensible heat flux for neutral, stable and unstable conditions while Figure 5.8 gives a comparison between measured sensible heat flux and MODIS based sensible heat flux for the entire data.

**Table 5.11: Validation of sensible heat flux over Ebro River basin, Spain (41°43’N, 0°49’W, elevation 225 m) for neutral conditions**

| Date | Time (local) | *In situ* measurements | | | $\bar{\varepsilon}$ | $\partial\varepsilon$ | $H_{MODIS}$ | $H_{MODIS}$- $H_{In\ situ}$ |
|---|---|---|---|---|---|---|---|---|
| | | H ($Wm^{-2}$) | $T_a$ (K) | $U_z$ ($ms^{-1}$) | | | | |
| 15/4/2004 | 2250 | -2.1 | 284.5 | 0.43 | 0.997 | 0.004 | -20.05 | -17.95 |
| 17/4/2004 | 2240 | -1.4 | 282.1 | 0.56 | 0.983 | -0.004 | -6.98 | -5.58 |
| 18/4/2004 | 1215 | 47.5 | 285.9 | 0.92 | 0.993 | -0.004 | 29.81 | -17.69 |
| 19/4/2004 | 2225 | -26.3 | 282.1 | 1.25 | 0.983 | -0.004 | 8.57 | 34.87 |
| 20/4/2004 | 2310 | -12.8 | 284.0 | 0.74 | 0.994 | -0.006 | 15.04 | 27.84 |
| 21/4/2004 | 2215 | -3.2 | 287.5 | 0.55 | 0.983 | -0.004 | -18.46 | -15.26 |
| 23/4/2004 | 1235 | 100.8 | 289.6 | 4.13 | 0.983 | -0.004 | 125.65 | 24.85 |
| 25/4/2004 | 2330 | -6.2 | 283.5 | 0.8 | 0.982 | -0.006 | 19.12 | 25.32 |
| 26/4/2004 | 2235 | -13.6 | 287.1 | 0.75 | 0.993 | -0.004 | 12.95 | 26.55 |
| 19/7/2004 | 2210 | -10.8 | 296.1 | 0.65 | 0.991 | -0.004 | 11.20 | 22.00 |
| 19/7/2004 | 2345 | -14.2 | 295.4 | 1.03 | 0.992 | -0.002 | 3.76 | 17.96 |
| 30/4/2004 | 2210 | -8.5 | 281.7 | 0.61 | 0.993 | -0.004 | -9.06 | -0.56 |
| 01/5/2004 | 2250 | -39.0 | 285.4 | 1.98 | 0.985 | -0.004 | -76.34 | -37.34 |
| 02/5/2004 | 2335 | -14.7 | 284.6 | 0.95 | 0.992 | 0.002 | -63.19 | -48.69 |
| 04/5/2004 | 2145 | -0.1 | 284.8 | 0.59 | 0.996 | -0.002 | -17.18 | -17.08 |
| 05/5/2004 | 2225 | -6.4 | 282.9 | 0.81 | 0.985 | -0.004 | -32.72 | -26.32 |
| 06/5/2004 | 2310 | -4.0 | 283.2 | 0.56 | 0.992 | -0.002 | -14.75 | -10.75 |
| 10/5/2004 | 2245 | -15.5 | 286.7 | 1.6 | 0.985 | -0.004 | -7.42 | 8.08 |
| 14/5/2004 | 2220 | -15.7 | 284.6 | 0.77 | 0.991 | -0.004 | 12.20 | 27.90 |
| 08/5/2004 | 2300 | -19.0 | 284.0 | 0.96 | 0.994 | -0.002 | 10.73 | 29.73 |
| 09/5/2004 | 2340 | -0.8 | 286.1 | 0.38 | 0.993 | 0.000 | -7.96 | -7.16 |

**Table 5.12: Validation of sensible heat flux over Ebro River basin, Spain (41°43'N, 0°49'W, elevation 225 m) for stable conditions**

| Date | Time (local) | *In situ* measurements | | | $\bar{\varepsilon}$ | $\partial\varepsilon$ | $H_{MODIS}$ | $H_{MODIS}$- $H_{In\ situ}$ |
|---|---|---|---|---|---|---|---|---|
| | | H ($Wm^{-2}$) | $T_a$ (K) | $U_z$ ($ms^{-1}$) | | | | |
| 16/4/2004 | 1230 | -7.8 | 284.2 | 4.12 | 0.993 | -0.004 | -0.3 | 7.50 |
| 16/4/2004 | 2335 | -38.9 | 285 | 4.33 | 0.991 | -0.004 | -40.7 | -1.83 |
| 28/4/2004 | 2220 | -37.3 | 283.8 | 1.99 | 0.987 | -0.004 | -18.3 | 19.00 |
| 18/7/2004 | 1200 | 220.0 | 305.4 | 1.48 | 0.993 | -0.004 | 133.2 | -86.80 |
| 18/7/2004 | 2305 | -18.9 | 296.5 | 3.35 | 0.983 | -0.004 | -23.0 | -4.09 |
| 30/4/2004 | 1240 | 207.5 | 290.1 | 3.37 | 0.991 | -0.004 | 136.6 | -70.87 |
| 30/4/2004 | 2345 | -8.4 | 281.6 | 0.68 | 0.994 | -0.002 | -50.9 | -42.49 |
| 03/5/2004 | 2240 | -56.5 | 285.1 | 4.22 | 0.994 | -0.002 | -82.9 | -26.39 |
| 11/5/2004 | 2330 | -68 | 286.3 | 3.28 | 0.993 | -0.004 | -17.4 | 50.62 |

**Table 5.13: Validation of sensible heat flux over Ebro River basin, Spain (41°43'N, 0°49'W, elevation 225 m) for unstable conditions**

| Date | Time (local) | *In situ* measurements | | | $\bar{\varepsilon}$ | $\partial\varepsilon$ | $H_{MODIS}$ | $H_{MODIS}$- $H_{In\ situ}$ |
|---|---|---|---|---|---|---|---|---|
| | | H ($Wm^{-2}$) | $T_a$ (K) | $U_z$ ($ms^{-1}$) | | | | |
| 20/4/2004 | 1205 | 189.5 | 292.9 | 4.7 | 0.989 | -0.004 | 133.0 | -56.62 |
| 26/4/2004 | 1125 | 178.0 | 290.0 | 1.0 | 0.983 | -0.004 | 249.2 | 71.21 |
| 29/5/2004 | 1200 | 90.8 | 287.2 | 3.2 | 0.994 | -0.006 | 23.7 | -67.1 |
| 09/5/2004 | 1235 | 146.4 | 293.2 | 1.29 | 0.983 | -0.004 | 127.3 | -19.1 |

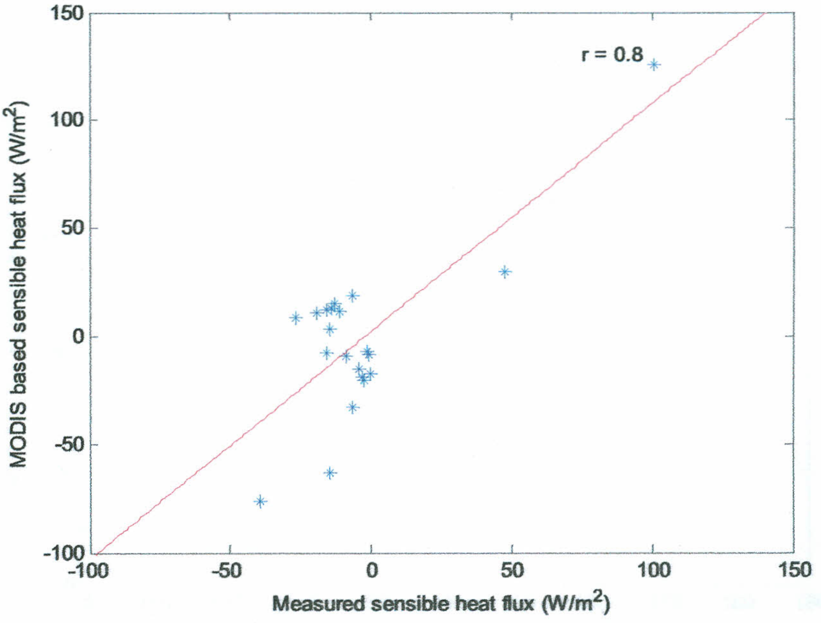

**Figure 5.5: Comparison between measured sensible heat flux and MODIS based sensible heat flux over Ebro River basin, Spain for neutral conditions**

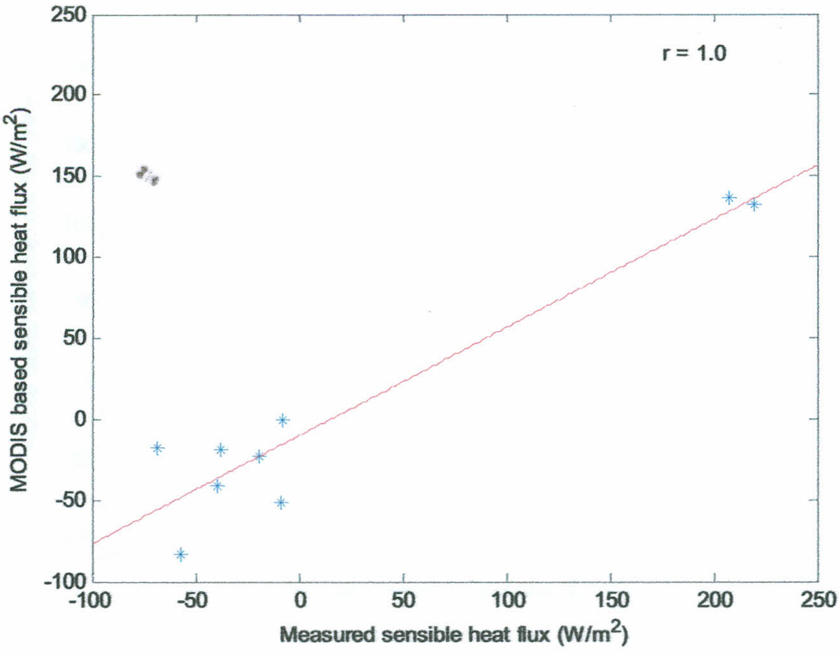

**Figure 5.6: Comparison between measured sensible heat flux and MODIS based sensible heat flux over Ebro River basin, Spain for stable conditions**

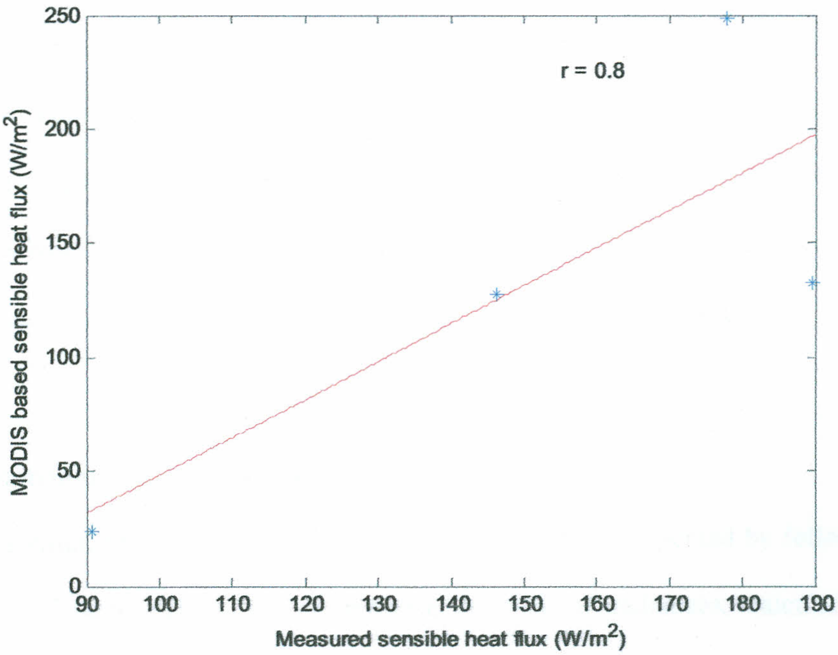

**Figure 5.7: Comparison between measured sensible heat flux and MODIS based sensible heat flux over Ebro River basin, Spain for unstable conditions**

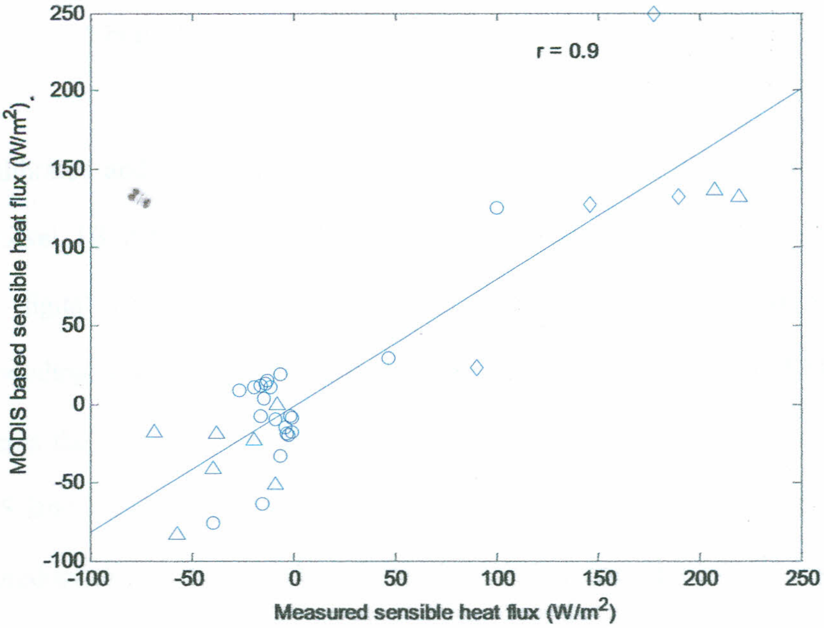

**Figure 5.8: Comparison between measured sensible heat flux and MODIS based sensible heat flux over Ebro River basin, Spain: Neutral (O); Stable (Δ) and Unstable (◊) conditions.**

From the figures, it is evident that sensible heat flux calculated shows a better agreement with the ground data. The correlation coefficients for neutral, stable and unstable conditions are 0.8, 1.0 and 0.8 respectively; resulting in an overall correlation coefficient of 0.9 for the entire data. Whatever the stability condition, MODIS based sensible heat flux and measured sensible heat flux were reasonably well correlated, but with a slight bias to stable atmospheric condition.

### 5.5 Algorithm implementation

The algorithm for estimating sensible heat flux can be implemented by following a number of steps. They include retrieval of spectral radiances, calculation of brightness temperatures corresponding to the radiances, ground based measurements and interpolation of air temperature and wind speed and finally the retrieval of the sensible heat flux taking into account atmospheric effects, emissivity effects and atmospheric stabilities.

The calibrated and geolocated spectral radiance, in $Wm^{-2}\mu m^{-1}sr^{-1}$, can be obtained from Level 1B data product (MOD021KM), generated from MODIS Level 1A sensor digital counts. Once the spectral radiances have been retrieved, the corresponding brightness temperatures may be derived from equation (3.8), which represents the inverse of the Planck formula around the central wave number $\upsilon$. MODIS land surface emissivities, appearing in the proposed algorithm, are derived from product (MOD11_L2). The proposed algorithm also requires knowledge of atmospheric water vapour. This product (MOD 05_L2) will be used explicitly in the algorithm if the atmospheric water vapor content of a region is above 3.0 g $cm^{-2}$ according to equation (5.29).

In addition to satellite data, ground based measurements of basic parameters including air temperature and wind speed are inevitable. Such data can preferably be obtained from weather station network and interpolated to scale from point and spatial observation to regional observation.

Anticipated applications of sensible heat flux data derived from the proposed algorithm include:

- Global climate studies and weather prediction
- Monitoring of other surface fluxes
- Energy changes research

# CHAPTER 6

# CONCLUSIONS AND RECOMMENDATIONS

Do not think lightly of good, that nothing will come of it. A whole water pot will fill up from dripping drops of water.

**Lord Buddha**

In Dhammapada (v 122)

## 6.1 Conclusions

The main objective of this research was to develop an algorithm which can be used to estimate sensible heat flux from remotely sensed Moderate Resolution Imaging Spectroradiometer (MODIS) data. This objective was achieved by following a number of steps earlier outlined as specific objectives. Different atmospheric effects were simulated, for the atmospheric situations considered, and used to determine coefficients appearing in the proposed algorithm

Land surface temperature was retrieved using a modified form of the GSWT proposed by Mito *et al.*, 2006 (equation 4.25). The modified GSWT retrieves $T_S$ taking into account surface and air temperature difference effects in addition to atmospheric water vapour and non–unitary surface emissivity. With the modified GSWT, the bulk aerodynamic equation and the resulting aerodynamic resistance equation, a general algorithm for estimating sensible heat flux from remotely sensed Moderate Resolution Imaging Spectroradiometer in two thermal bands, 10.780 μm–11.280 μm and 11.770 μm–12.270 μm has been developed (equation 5.27).

Coefficients which take into account different atmospheric conditions have been determined, by linear regression analysis with least–square–sum fitting using 21 sets of emissivities. Since they were found to be scarcely influenced by the atmospheric water vapour content less than or equal to 3.0 g cm$^{-2}$, their mean values ($k_1 = 61.92$, $k_2 = -125.47$ and $k_3 = 48.63$) were considered. For any realistic amount of atmospheric water vapour above 3.0 g cm$^{-2}$, coefficients used to estimate sensible heat flux were found to be linear functions of atmospheric water vapour column, equation 5.28.

The advantage of this algorithm, unlike other conventional methods earlier developed for determination of sensible heat flux, is that a prior knowledge of surface temperature as an auxiliary input is not necessary. With aerodynamic resistance computed from canopy properties, emissivities and water vapor column determined from satellite data, air temperature becomes the only auxiliary measurement required to compute sensible heat flux in this new algorithm.

Sensible heat flux has been validated with *in situ* data from Ebro River basin, Spain for the year 2004 for different days ranging from 15th April, 2004 to 26th July, 2004. MODIS based sensible heat flux was found to be highly correlated to measured sensible heat flux, with an overall correlation coefficient for all the three conditions being 0.9.

## 6.2 Recommendations

Future work will involve evaluating other energy balance components including latent heat flux, ground heat flux and net radiation based on results obtained from this algorithm. This will provide a greater insight on the algorithm's reliability in evaluating the energy balance components and hence its applicability in modeling and monitoring these components.

The general algorithm developed estimates sensible heat flux as a function of surface emittance effect, water vapor column (WVC), canopy properties, air temperature and different atmospheric stabilities. However air temperature is not available by remote sensing. *In situ* measurement of $T_a$ on large scale is expensive, time consuming and difficult. Future work may therefore involve evaluating sensible heat flux without prior knowledge of air temperature. This is expected to increase the accuracy of retrieval of sensible heat flux from satellite data.

# REFERENCES

Abreham, A. (2009). Open water Evaporation Estimation using ground measurement and satellite remote sensing: a case study of Lake Tana, Ethiopia. *M.Sc Thesis* (*Geo–information and Earth Observation*). International Institute for Geo–information Science and Earth Observation. Netherlands.

Allen, R.G., Tasumi, M., Morse, A. and Trezza, R. (2005). A Landsat–based energy balance and evaporation model in Western US Water Rights Regulation and Planning. *Journal of Irrigation and Drainage systems*. **19**: 251–268.

Anandakumar, K. (1999). Sensible heat flux over a wheat canopy: Optical scintillometer measurements and surface renewal analysis estimations. *Agricultural and Forest Meteorology*. **96**: 145–156.

Cain, J.D., Rosier, P.T.W., Meijninger, W. and De Bruin, H.A.R. (2000). Spatially averaged sensible heat fluxes measured over barley. *Agriculture and Forest Meteorology*. **107**: 307–322.

Castellvi, F. and Martínez-Cob, A. (2005). Estimating sensible heat flux using surface renewal analysis and the flux variance method: A case study over olive trees at Sástago (NE of Spain).Water Resources Research, **41**, W09422, doi: 10.1029/2005WR004035.

Chehbouni, A., Loseen, D., Njoku, E.G., Lhomme, J.P., Monteny, B. and Kerr, Y.H. (1997). Examination of difference between radiative and aerodynamic surface temperature over sparsely vegetated surfaces. *Remote Sensing of the Environment*. **58**: 177–186.

Chehbouni, A., Watts, C., Lagouarde, J.P., Kerr, Y.H., Rodriguez, J.M., Bonnefond, F., Santiago, G., Dedieu, D.C., Goodrich, C. and Unkrich, T (2000). Estimation of heat and momentum fluxes over complex terrain using a large aperture scintillometer. *Agricultural and Forest Meteorology*. **105**: 215–225.

Choudhury, B. J. and Monteith, J. L. (1988). A four layer model for the heat budget of homogeneous land surfaces, Quart. *J.Roy. Meteorol. Soc.*. **11**: 373–398.

Choudhury, B.J., Reginato, R.J. and Idso, S.B. (1986). An analysis of infrared temperature observations over wheat and calculation of latent heat flux. *Agric. Meteorol.*. **37**: 75–88.

De Bruin, H.A.R., Nieveen, J.P., De Wekker, S.F.J, Heusinkveld, B.G. (1996). Large aperture Scintillometry over a 4.8 km path for measuring a really–average sensible heat flux. In proceedings on the 22nd AMS Symposium on Agricultural and Forest Meteorology, 28th January–2nd February. Antlanta, GA. U.S.A.

De Wekker, S.F.J. (1996). The estimation of a really–averaged Sensible heat fluxes over complex terrain with a Large-Aperture Scintillometer. *M.Sc. Thesis*. Department of Meteorology, Wageningen Agricultural University.

García, M. and Sergio, C. (2005). Estimating land surface energy fluxes in SE Spain using ASTER and MODIS data. *Journal of Remote Sensing*. **26**: 1–9.

García, M., Fernández, F., Villagarcía, L., Palacios-Orueta, A., Were, A., Puigdefábregas, J. and Domingo, F. (2008). Estimating latent and sensible heat fluxes using the temperature vegetation dryness index (TVDI) and MODIS data. *IEEE Transactions on Geoscience and Remote Sensing*. **3**, 867-870.

Hall, G.H., Huemmrich, K.F., Goetz, S.J., Sellers, P.J. and Nickeson, J.E. (2008). Satellite remote sensing of surface energy balance: success, failure and unresolved issues in FIFE. *Journal of Geophysical Research*. **97**: 19061–19089.

Houghton, J.T., Ding, Y., Griggs, D.J., Noguer, M., Van Der Linden, P.J. and Dai, X. (2001). Climate change 2001: The scientific basis. Cambridge University Press, Cambridge, UK.

Jiayi, P., Yan, X.H., J.O. and Zheng, Q. (2003). A New Method for Estimation of the Sensible Heat Flux under Unstable Conditions Using Satellite Vector Winds. *Journal of Physical Oceanography*. **34**: 968–977.

Kabsch E. (2009). Validation of Land surface temperatures from MSG satellite measurements by observations at the ground station near Evora. *P.H.D Thesis* (*Remote sensing*). Portugal.

Kustas, W.P. and Craig, C.S.T. (1990). Estimation of the soil heat flux/net radiation ratio from spectral data. *Agricultural and Forest Meteorology*. **49**: 205–223.

Kustas, W.P. (1989). Estimating Surface Energy–Balance components from Remotely Sensed data. In Theory and Applications of Optical Remote Sensing, G. Asrar (Ed.), pp. 604–627 (New York: A Wiley Interscience).

Liu, S., Mao, D. and Jia, L. (2007). Evaluating Parameterization of aerodynamic resistance to heat transfer using field measurements. *Hydrology and Earth System Sciences*. **11**: 769–783.

Lu, L. (2009). Modeling surface temperature under clouds using geo–stationary satellite observations. *M.Sc. Thesis (Geo–Information Science and Earth Observation)*. University of Southampton. UK.

Mallick, K., Bhattacharya, B.K., Rao, V.U.M., Reddy, D., Banerjee, S., Venkatesh, H., Pandey V., Kar, G., Mukherjee, J., Vyas, S.P., Gadgil, A.S. and Patel, N.K. (2009). Latent heat flux estimation in clear sky days over Indian agro ecosystems using noontime satellite remote sensing data. *Agricultural and Forest Meteorology*, **149**, 1646–1665.

Meijninger, W.M.L and De Bruin, H.A.R. (1999). The sensible heat fluxes over irrigated areas in western Turkey determined with a large aperture Scintillometer. *Journal of Hydrology*. **229**: 42–49.

McMillin, L.M. (1975). Estimation of Sea Surface Temperatures from Two Infrared Window Measurements with Different Absorption. *Journal of Geophysical Research*. **80**: 5113–5117.

McMillin, L. M. (1980). The split window algorithm for sea surface temperature derived from satellite measurements. In *Remote Sensing of Atmospheres and Oceans*,edited by A.Deepak (London: Academic Press), 437-455. Deepak (London: Academic Press), 437–455.

Mito, C. O. (2002). Retrieval of land and sea surface temperatures using MODIS data with improved split window technique. *Ph.D. Thesis (Physics)*. University of Rome. Italy.

Mito, C.O., Laneve, G., Castronuovo, M.M. and Ulivieri, C. (2006). Derivation of land surface temperatures from MODIS data using the general split–window technique. *International Journal of Remote Sensing*. **27**: 2541–2552.

Ouaidrari H., Goward S.N., Czajkowski K.P., Sobrino J.A., Vermote E. (2002). Land Surface Temperature estimation from AVHRR thermal infrared measurements: An assessment for the AVHRR Land Pathfinder II data set. *Remote sensing of environment*. **81**: 114–128.

Paw, U., Qui, J., Su, H.B., Watanable, T. and Brunet, Y. (1995). Surface renewal analysis: a new method to obtain scalar fluxes. *Agric. For. Meteorology*. **74**: 119–137.

Pidwirny M. (2006). Net Radiation and the Planetary Energy Balance: Fundamentals of Physical Geography, 2nd Edition. Available online http://www.physicalgeography.net/findamentals/7i.html (accessed 14 September, 2011).

Samuel, O., Ortega, F., Richard, H. and Ek M. (1996). Daytime variation of sensible heat flux estimated by bulk aerodynamic method over grass canopy. *Agricultural and Forest Meteorology*. **81:** 131–143.

Schowengerdt, R.A. (2007). Remote Sensing: Models and methods for Image processing. (Third edition). Academic Press, Califonia, USA.

Sobrino, J.A, Li, Z. L and Stoll, M.P. (1993). Impact of the Atmospheric Transmittance and Total Water Vapor Content in the Algorithms for Estimating Satellite Sea Surface Temperatures. *IFFE transactions on geoscience and remote sensing*. **31**: 946–952.

Sobrino, J.A., Julien, Y., Hidalgo, V., Jimenez, J.C., Soria, G., Mattar, C., Franch, R. and Oltra, J. (2008). Estimation of land surface temperature using AVHRR sensors on the NOAA satellite. *Technical Report.* **9**: 1–14.

Tang B., Bi Y., Li., Z and Xia J. (2008). Generalized Split–window algorithm for estimate of land surface temperature from Chinese Geostationary Feng Yun Meteorological Satellite (FY–2C) data. **8**: 933–951.

Ulivieri, C. (1984). Minimization of atmospheric water vapour and surface emittance effects on remotely sensed sea surface temperatures. *IEEE Transactions on Geoscience and Remote Sensing*. **22**: 622–628.

Ulivieri, C. and Cannizzaro G. (1985). Land surface temperature retrievals from satellite measurements. Acta Astronautica, **12**, 977–985.

Ulivieri, C., Castronuovo, M.M., Francioni, R. and Cardillo, A. (1994). A split window algorithm for estimating land surface temperature from satellites. *Advances in space Research*. **14**: 59–65.

Wan, Z. and Dozier, J. (1989). Land surface temperature measurement from space: physical principles and inverse modeling. *IEEE Transactions on Geoscience and Remote Sensing*. **27**: 268–278.

Wan, Z. and Li, Z.L. (1997). A Physics–based algorithm for retrieving surface emissivity and temperature from EOS/MODIS data. *IEEE Transactions on Geoscience and Remote Sensing.* **34**: 980–996.

Wang, K. and Liang S. (2009). Evaluation of ASTER and MODIS land surface temperature and emissivity products using long–term surface longwave radiation observations at SURFRAD sites. *Journal of Remote Sensing of Environment*. **113**: 1556–1565.

Watts, C., Chehbouni, A., Kerr, Y.H., Bruin, H.R., Hartogensis, O. and Rodriguez, J. (1998). Sensible heat flux estimates using AVHRR and scintilllometer data over grass and mesquite in Northwest Mexico. Available online at:http://www.tucson.ars.ag.gov/salsa/archive/publications/ams_preprints/watts.html (accessed 14 September, 2011).

Watts, C., Chehbouni, A., Kerr, Y.H., Bruin, H.R., Hartogensis, O. (2000). Comparison of sensible heat flux estimates using AVHRR with scintillometer measurements over semi–arid grassland in northwest Mexico. *Agricultural and Forest Meteorology*. **105**: 81–89.

Xiong, X., Chiang, K.F., Barnes, W. L., Guenther, B. and Salomonson, V.V. (2008). Multiyear on–orbit calibration and performance of Terra MODIS thermal emissive bands. *Transactions on Geoscience and Remote Sensing*. **46**: 1790−1803.

Yamaguchi, Y., Kato, S., and Okamoto, K. (2004). Surface heat flux analysis in urban areas using ASTER and MODIS data. International Symposium on GeoInformatics for Spatial-Infrastructure Development in Earth and Allied Sciences: GIS-IDEAS. 2004, Hanoi, Vietnam. Available online at: http://gisws.media.osaka-cu.ac.jp/gisideas04/viewpaper.php?id=34 (accessed 14 September, 2011).

# APPENDICES

## Appendix 1: A section of a program used in computing atmospheric variables

```
clear
% This first part loads dataset used in computation. The dataset was simulated from
the PcLnWin software using radiative transfer equation
load AVHRR4.txt
load AVHRR5.txt
load MODIS31.txt;
load MODIS32.txt;
load wv1.txt    %Loads data set containing watervapor for first simulation in
moles/cm2
load downlooking31.txt %loads data set 12 for band 31 sensor downlooking
load downlooking32.txt %loads data set 12 for band 32 sensor downlooking
load uplooking31.txt   %loads data set 11 for band 31 sensor uplooking
load uplooking32.txt   %loads data set 11 for band 32 sensor uplooking
load stemps.txt        %loads the value of first boundary temp
load band31e1r0Ts.txt
%This second program assigns standard constants used in the study
C1=1.1910659e-12;       % First radiation co nstant in Watts cm^2 sr-1
C2=1.438833;            % Second radiation constant in cm K
n1=6.022169e+23;        %Expression of Avogadros constant
n2=18;                  % molecular mass of water
nu31=906.6183;          % central wavenumber band 31  cm-1
nu32=831.9468;         % central wavenumber band 32  cm-1
norm31=0.514603;        % normalization factor for band 31 derived from simulation
norm32=0.621434;        % normalization factor for band 32 derived from simulation
%Emissivity for MODIS bands 31 and 32 are assigned 1 (case 1) and 0.9 (case 2)
e31prm=1;
e32prm=1;
e31=0.89;
e32=0.91;
delle=e31-e32;
```

```
ebar=(e31+e32)/2;
%This third part of the programme converts simulated watervapor from moles/cm2 to g/cm2
for i=1:27
wv2(i)=wv1(i)*n2/n1;
end
%This fourth part of the programme evaluate downwelling and upwelling atmospheric mean radiances and the ratios Z31 and Z32
for i=1:27
t31(i)=downlooking31(i,1);
t32(i)=downlooking32(i,1);  %Intergrated transmittance for MODIS band 31
meanupwelling31(i)=(downlooking31(i,2)/norm31)/(1-t31(i));
meandownwelling31(i)=(uplooking31(i,2)/norm31)/(1-t31(i));
meanupwelling32(i)=(downlooking32(i,2)/norm32)/(1-t32(i));
meandownwelling32(i)=(uplooking32(i,2)/norm32)/(1-t32(i));
Z31(i)=meandownwelling31(i)/meanupwelling31(i);
Z32(i)=meandownwelling32(i)/meanupwelling32(i);
end
%This fifth part of the programme evaluates components of c(i) and hence c(i)
for i=1:27;
B1Tair(i)=C1*nu31^3/(exp(C2*nu31/stemps(i))-1.);
%Ta31(i)=C2*nu31/log(1.+(C1*nu31^3)/meanupwelling31(i));%Test
Ta32(i)=C2*nu32/log(1.+(C1*nu32^3)/meanupwelling32(i));
%B1T1bar(i)=C1*nu31^3/(exp(C2*nu31/Ta31(i))-1.);
B1T2bar(i)=C1*nu31^3/(exp(C2*nu31/Ta32(i))-1.);
B1T1bar(i)=meanupwelling31(i);
diff1(i)=B1Tair(i)-B1T2bar(i);
diff2(i)=B1Tair(i)-B1T1bar(i);
c(i)=diff1(i)/diff2(i);
c(i)=1.04;% Mean of c
end
%This sixth part of the programme computes ai'and ai (emissivities beind 1 and 0.9 for the two bands respectively)
for i=1:27;
```

```
A31prm(i)=1-t31(i);
A32prm(i)=1-t32(i);
E31prm(i)=t31(i);
E32prm(i)=t32(i);
Dstarprm(i)=c(i)*A32prm(i)*(A31prm(i)+E31prm(i))-
A31prm(i)*(A32prm(i)+E32prm(i));
a1prm(i)=(c(i)*A32prm(i)-A31prm(i))/Dstarprm(i);
a2prm(i)=A31prm(i)/Dstarprm(i);
a3prm(i)=(c(i)-1)*A31prm(i)*A32prm(i)/Dstarprm(i);
%This is the end of evaluation of ai'
end
for i=1:27;
A31(i)=(1-t31(i))*(1+(1-e31)*t31(i)*Z31(i));
A32(i)=(1-t32(i))*(1+(1-e32)*t32(i)*Z32(i));
E31(i)=e31*t31(i);
E32(i)=e32*t32(i);
Dstar(i)=c(i)*A32(i)*(A31(i)+E31(i))-A31(i)*(A32(i)+E32(i));
a1(i)=(c(i)*A32(i)-A31(i))/Dstar(i);
a2(i)=A31(i)/Dstar(i);
a3(i)=(c(i)-1)*A31(i)*A32(i)/Dstar(i);
%This is the end of evaluation of ai'
end
for i=1:27;
A31(i)=(1-t31(i))*(1+(1-e31)*t31(i)*Z31(i));
A32(i)=(1-t32(i))*(1+(1-e32)*t32(i)*Z32(i));
E31(i)=e31*t31(i);
E32(i)=e32*t32(i);
Dstar(i)=c(i)*A32(i)*(A31(i)+E31(i))-A31(i)*(A32(i)+E32(i));
a1(i)=(c(i)*A32(i)-A31(i))/Dstar(i);
a2(i)=A31(i)/Dstar(i);
a3(i)=(c(i)-1)*A31(i)*A32(i)/Dstar(i);
%This is the end of evaluation of ai
end
%This seveth part of the program computes brightness temp for bands 31 and 32
```

```
for i=1:27;
Tb31(i)=C2*nu31/log(1.+(C1*nu31^3*norm31)/band31e1r0Ts(i,2));
Tb32(i)=C2*nu32/log(1.+(C1*nu32^3*norm32)/band32e1r0Ts(i,2));
Tbdiff(i)=Tb31(i)-Tb32(i);             %difference in the brightness temperatures
Tsprm(i)=Tb31(i)+a2prm(i)*Tbdiff(i);
%This is the end of evaluation of Tb31 and Tb32
end
%This ninth part of the program evaluates the beta term
for i=1:27;
m1(i)=(C2*nu31)/Tb31(i);
m2(i)=1/m1(i);
beta(i)=m2(i)*(exp(m1(i))-1)/exp(m1(i));
BM=mean(beta);
%This is the end of evaluation of beta(i)
D1(i)=c(i)*A32prm(i)-A31prm(i);
D2(i)=(A32prm(i)*(E32prm(i)*Z32(i)-E31prm(i)*(1-
A31prm(i)*Z31(i)))*c(i))+(A31prm(i)*(E32prm(i)*(1-A32prm(i)*Z32(i))-
E31prm(i)*Z31(i)));
D3(i)=0.5*((A32prm(i)*(E32prm(i)*Z32(i)+E31prm(i)*(1-
A31prm(i)*Z31(i)))*c(i))+(A31prm(i)*(E32prm(i)*(1-
A32prm(i)*Z32(i))+E31prm(i)*Z31(i))));
D4(i)=A32prm(i)*E31prm(i)*E32prm(i)*Z32(i)*(A31prm(i)*Z31(i)-
1)*c(i)+A31prm(i)*E32prm(i)*E31prm(i)*Z31(i)*(1-A32prm(i)*Z32(i));
D(i)=D1(i)+D2(i)*(1-ebar)+D3(i)*(delle)+D4(i)*((1-ebar)^2-(0.5*delle)^2);
G4a(i)=A31prm(i)*A32prm(i)*(c(i)-1);
G4b(i)=c(i)*A31prm(i)*A32prm(i)*(E32prm(i)*Z32(i)+E31prm(i)*Z31(i))-
A31prm(i)*A32prm(i)*(E32prm(i)*Z32(i)+E31prm(i)*Z31(i));
G4c(i)=0.5*(c(i)*A31prm(i)*A32prm(i)*(E32prm(i)*Z32(i)-E31prm(i)*Z31(i))-
A31prm(i)*A32prm(i)*(E32prm(i)*Z32(i)-E31prm(i)*Z31(i)));
G4d(i)=A31prm(i)*A32prm(i)*E31prm(i)*E32prm(i)*Z31(i)*Z32(i)*(c(i)-1);
G4(i)=G4a(i)+G4b(i)*(1-ebar)+G4c(i)*(delle)+G4d(i)*((1-ebar)^2-(0.5*delle)^2);
end
for i=1:27;
k1(i)=(A31prm(i)*Z31(i)-1)*c(i);
```

```
k2(i)=(1-A32prm(i).*Z32(i));
k3(i)=(1+Z31(i)*E31prm(i));
k4(i)=A32prm(i)*E31prm(i);
k5(i)=A31prm(i)*E32prm(i);
k6(i)=E32prm(i)*Z32(i);
k7(i)=E31prm(i)*E32prm(i);
k8(i)=A32prm(i)*Z32(i);
k9(i)=A31prm(i)*Z31(i);
k10(i)=(1-A31prm(i)*Z31(i));
k11(i)=E31prm(i)*Z31(i);
k12(i)=A32prm(i)*E31prm(i)*E32prm(i)*Z32(i);
k13(i)=A31prm(i)*E32prm(i)*E31prm(i)*Z31(i);
k14(i)=(A31prm(i)*A32prm(i)*(E32prm(i)*Z32(i)+E31prm(i)*Z31(i))*c(i))-
(A31prm(i)*A32prm(i)*(E32prm(i)*Z32(i)+E31prm(i)*Z31(i)));
k15(i)=(A31prm(i)*A32prm(i)*(E32prm(i)*Z32(i)-E31prm(i)*Z31(i))*c(i))-
(A31prm(i)*A32prm(i)*(E32prm(i)*Z32(i)-E31prm(i)*Z31(i)));
k16(i)=(A32prm(i)*(k6(i)+E31prm(i)*k10(i))*c(i))+(A31prm(i)*(E32prm(i)*k2(i)+
k11(i)));
k17(i)=A31prm(i)*A32prm(i)*E31prm(i)*E32prm(i)*Z31(i)*Z32(i)*(c(i)-1);
G1(i)=(-1*beta(i)*(k4(i)*k1(i)+k5(i)*k2(i))*Tb31(i))-
(a2prm(i)*(A32prm(i)*(k6(i)*-E31prm(i)*k3(i))*c(i)+k5(i)*k2(i))*Tbdiff(i));
G2(i)=0.5*(beta(i)*(k4(i)*k1(i)-k5(i)*k2(i))*Tb31(i)+a2prm(i)*(A32prm(i)*(-
1*k6(i)-E31prm(i)*k3(i))*c(i)-k5(i)*k2(i))*Tbdiff(i));
G3(i)=(-1*beta(i)*(k7(i)*(k8(i)*k1(i)+k9(i)*k2(i)))*Tb31(i))-
(a2prm(i)*(k7(i)*(k8(i)*k1(i)+k9(i)*k2(i)))*Tbdiff(i));
F1(i)=G1(i)/D(i);
F2(i)=G2(i)/D(i);
F3(i)=G3(i)/D(i);
F4(i)=G4(i)/D(i);
S1(i)=F1(i)/(1-F4(i))
S2(i)=F2(i)/(1-F4(i));
S3(i)=F3(i)/(1-F4(i));
end
```

## Appendix II: Emissivity data set used in the estimation of $k_1$, $k_2$ and $k_3$, (Mito *et al.*, 2006)

| $\bar{\varepsilon}$ | $\varepsilon_1$ | $\varepsilon_2$ | $(1-\bar{\varepsilon})$ | $\delta\varepsilon$ | $(1-\bar{\varepsilon})^2-(0.5\delta\varepsilon)^2$ |
|---|---|---|---|---|---|
| 0.98 | 0.99 | 0.97 | 0.02 | 0.02 | 0.00030000 |
| | 0.985 | 0.975 | | 0.01 | 0.00037500 |
| | 0.9825 | 0.9775 | | 0.005 | 0.00039375 |
| | 0.98 | 0.98 | | 0.0 | 0.00040000 |
| | 0.9775 | 0.9825 | | -0.005 | 0.00039375 |
| | 0.975 | 0.985 | | -0.01 | 0.00037500 |
| | 0.97 | 0.99 | | -0.02 | 0.00030000 |
| 0.94 | 0.95 | 0.93 | 0.06 | 0.02 | 0.00350000 |
| | 0.945 | 0.935 | | 0.01 | 0.00357500 |
| | 0.9425 | 0.9375 | | 0.005 | 0.00359375 |
| | 0.94 | 0.94 | | 0.0 | 0.00360000 |
| | 0.9375 | 0.9425 | | -0.005 | 0.00359375 |
| | 0.935 | 0.945 | | -0.01 | 0.00357500 |
| | 0.93 | 0.95 | | -0.02 | 0.00350000 |
| 0.9 | 0.91 | 0.89 | 0.10 | 0.02 | 0.00990000 |
| | 0.905 | 0.895 | | 0.01 | 0.00997500 |
| | 0.9025 | 0.8975 | | 0.005 | 0.00999375 |
| | 0.9 | 0.9 | | 0.0 | 0.01000000 |
| | 0.8975 | 0.9025 | | -0.005 | 0.00999375 |
| | 0.895 | 0.905 | | -0.01 | 0.00997500 |
| | 0.89 | 0.91 | | -0.02 | 0.00990000 |